A two-component vector WIMP — fermion FIMP dark matter model with an extended seesaw mechanism

Francesco Costa,[a] **Sarif Khan**[a,*] **and Jinsu Kim**[b,c,*]

[a]*Institute for Theoretical Physics, Georg-August University Göttingen,*
Friedrich-Hund-Platz 1, Göttingen D-37077, Germany

[b]*School of Physics Science and Engineering, Tongji University,*
Shanghai 200092, China

[c]*Theoretical Physics Department, CERN,*
1211 Geneva 23, Switzerland

E-mail: francesco.costa@theorie.physik.uni-goettingen.de,
sarif.khan@uni-goettingen.de, jinsu.kim@cern.ch

Abstract: We consider an extension of the Standard Model that explains the neutrino masses and has a rich dark matter phenomenology. The model has two dark matter candidates, a vector WIMP and a fermion FIMP, and the sum of their relic densities matches the total dark matter abundance. We extensively study the dark matter production mechanisms and its connection with the neutrino sector, together with various bounds from present and future experiments. The extra scalar field in the model may induce a first-order phase transition in the early Universe. We study the production of stochastic gravitational waves associated with the first-order phase transition. We show that the phase transition can be strong, and thus the model may satisfy one of the necessary conditions for a successful electroweak baryogenesis. Detectability of the phase transition-associated gravitational waves is also discussed.

---

*Corresponding author.

Contents

1 Introduction

The Standard Model (SM) of particle physics has proved extremely successful in the past decades with the experiments matching its predictions and the Higgs boson discovery being the final piece to complete it. Nonetheless, astrophysical and cosmological evidence have posed questions that are not explained by the SM and are still open problems to this date.

It is well established by neutrino oscillation data (NOD) that the neutrinos have a non-zero mass while in the SM they are massless. A mechanism is therefore needed to

generate the masses [1, 2]. The neutrinos are not only massive, but their masses are also much lighter than the other matter particles. The mass splitting between the first and the second eigenstates is $|\Delta m_{21}^2| = 7.42^{+0.21}_{-0.20} \times 10^{-5} \, \text{eV}^2$, and the mass gap between the second and the third is $\Delta m_{32}^2 = 2.517^{+0.026}_{-0.028} \times 10^{-3} \, \text{eV}^2$ [3]. Also, from cosmological data, the sum of the neutrino masses is bounded by $\sum_i m_{\nu_i} < 0.23 \, \text{eV}$ [4, 5]. These observations are calling for a new mechanism. Arguably the easiest and first proposed mechanism is the so-called type-I seesaw [6, 7], where heavy singlet leptons are introduced: The mixing between the heavy singlet leptons and the light neutrinos can generate a small mass since the light neutrino masses are suppressed by the heavy mass scale, resulting in $m_\nu \sim yv/M$ where M is of the order of the heavy lepton mass, v is the SM Higgs vacuum expectation value (VEV), and y is the light neutrino Yukawa coupling.

An extended version of the type-I seesaw mechanism, dubbed extended double seesaw [8, 9], where a second set of singlet neutrinos is added, was proposed to achieve a low-scale leptogenesis without a fine tuning of the heavy neutrino masses; see also ref. [10] for an ultraviolet (UV) completion. The attractiveness of the low-scale leptogenesis is its detection possibilities from future collider experiments. In addition, the supersymmetric version of the extended double seesaw mechanism avoids the gravitino problem [8, 11]; see also ref. [12]. Notably, the double seesaw mechanism allows us to consider Yukawa couplings for the extra neutrinos up to $O(1)$ with masses at the TeV scale, having the possibility to be probed by future collider experiments.

The dark matter (DM) is another missing piece of the SM. We have cosmological evidences that indicate that our Universe is composed of 23% of DM. These observations point towards cold, dark, and particle-like explanations [5, 13, 14]. The standard solution to the problem is a Weekly Interacting Massive Particle (WIMP) which is initially in thermal contact with the SM thermal bath in the early Universe. At some later time, it freezes out, producing the relic density observed today that is inversely proportional to the thermal cross section [15–18].

Alternative mechanisms have been explored with increasing interest since the effort to detect a WIMP-like particle has been unsuccessful up to now [19–24]. In particular, the freeze-in mechanism has gained tremendous attention in the past two decades [25–46]. The DM particle in this case is called a Feebly Interacting Massive Particle (FIMP) because its interaction is in general much smaller than the electroweak scale, with couplings $\lesssim \mathcal{O}(10^{-8})$. The tiny coupling is due to the requirement that the FIMP remains out-of-equilibrium during the history of the Universe.[1] The DM abundance is then produced by the out-of-equilibrium scattering or decay processes. When the particles are produced via operators of dimension higher than four, the production mechanism may be of the so-called UV freeze-in type where the relic density is mostly produced at the reheating temperature T_R. This is in stark contrast with the standard infrared (IR) freeze-in where the main production occurs at $T \sim m_{\text{FIMP}}$ where m_{FIMP} is the FIMP mass scale [30]. As we shall discuss later, in the model we study in this work, operators of dimension five give UV contributions to the relic density before the spontaneous symmetry breaking. After the symmetry breaking,

---

[1]Such a tiny coupling may naturally be realised in a clockwork framework [47–49]; see, e.g., refs. [50–52].

the dimension-5 operators also give IR contributions, dominated by the Higgs decay. The dominant contribution will depend on values of the Higgs mass, the reheating temperature T_R, and the scale of new physics Λ.

The visible sector described by the SM is composed of a complex arrangement of particles and gauge groups. Likewise, we could expect the similar complexity to arise in the dark sector. There is no experimental indication that the DM sector is composed of a single field. Since both the freeze-in and freeze-out mechanisms are viable production mechanisms, both the WIMP and FIMP could have been active in the early Universe, producing parts of the total DM relic density $\Omega_{\text{Tot}} h^2 = 0.120 \pm 0.001$ as observed by the Planck experiment [5]. Although the simplest setup would be the case where there are two DM candidates both of which contribute to the total DM relic abundance, one may consider a more general multi-component DM scenarios. Recent studies on the multi-component DM scenarios include refs. [53–94].

In this paper, we consider a beyond the SM (BSM) scenario that addresses the afore-mentioned problems, exploring its viability and the possible experimental signatures. We introduce two sets of three-generation extra neutrinos N_L^i and S_L^i where the first two generations of neutrinos are used in the extended seesaw mechanism to explain the light neutrino masses while the third generation will be part of the dark sector. In the mass basis, through mixing, N_m^3 and S_m^3 become FIMP-type particles, and considering S_m^3 to be the lighter one, it may become a viable DM candidate. We shall explore possible connections between the neutrino parameters and the DM relic density. The second DM candidate is the vector gauge boson W_D associated with an extra dark $U(1)_D$ gauge symmetry. We study constraints from the lepton flavour violation (LFV) data to the mixing angles and to the DM production via the neutrinos sector.

The dark Higgs field ϕ_D associated with the extra dark $U(1)_D$ modifies the scalar sector with respect to the SM. The evolution of the vacuum state may thus change, opening possibilities of having a first-order phase transition (FOPT). We show that the FOPT can be strong and discuss the detectability of the associated stochastic gravitational waves (GWs) [95] by future space-based observatories such as LISA [96], DECIGO [97–101], and BBO [102–104]. Recent work on the subject includes e.g. refs. [88, 94, 105–121]. This is an exciting possibility that opens an experimental window on the cosmological implication of the BSM model we present and may complement the study of (in-)direct detections and collider searches that may probe the nature of DM.

The rest of the paper is organised as follows. In section 2, we present the model under consideration in detail and explain the generation of the neutrino masses as well as the DM candidates. We then scrutinise the LFV bounds on the neutrino sectors in section 3. In section 4, we study the two-component DM scenarios and present the result together with various detection bounds. In section 5, possibilities of having a FOPT are explored. We also discuss the detectability of the stochastic GW signals associated with the FOPTs. In doing so, we present three benchmark points (BPs) that realise the neutrino masses, the correct DM relic density, a strong FOPT, and a detectable GW signal at the same time. Finally, we discuss potential collider searches in section 6 before we conclude in section 7.

2 Model

We consider the following Lagrangian

$$\mathcal{L} = \mathcal{L}_{\text{SM}} + \mathcal{L}_N + \mathcal{L}_{\text{DM}} + (D_\mu \phi_D)^\dagger (D^\mu \phi_D) - \frac{1}{4} F_D^{\alpha\beta} F_{D\alpha\beta} - \frac{\zeta}{2} F_D^{\alpha\beta} B_{\alpha\beta} - V(\phi_h, \phi_D) \,, \quad (2.1)$$

where $\mathcal{L}_{\text{SM}}$ is the SM Lagrangian with the SM Higgs field ϕ_h, $\mathcal{L}_N$ is the Lagrangian associated with the additional singlet neutrinos which take part in the neutrino masses, and $\mathcal{L}_{\text{DM}}$ corresponds to the DM Lagrangian. The fourth term describes the kinetic term for the extra $\text{U}(1)_D$ Higgs ϕ_D, and the covariant derivative is given by $D_\mu = \partial_\mu - i g_D W_{D\mu}$ with g_D being the $\text{U}(1)_D$ gauge coupling and W_D the vector boson associated with the extra $\text{U}(1)_D$ gauge symmetry. $F_D^{\alpha\beta}$ is the field strength of the vector boson W_D, $B^{\alpha\beta}$ is the field strength tensor associated with the hypercharge $\text{U}(1)_Y$ gauge group, and the gauge kinetic mixing between these two field strength tensors is parametrised by ζ. Finally, the last term represents the scalar potential which is given by

$$V(\phi_h, \phi_D) = \mu_D^2 \phi_D^\dagger \phi_D + \lambda_D (\phi_D^\dagger \phi_D)^2 + \lambda_{hD} (\phi_h^\dagger \phi_h)(\phi_D^\dagger \phi_D) \,. \quad (2.2)$$

The neutrino sector is described by

$$\mathcal{L}_N = \sum_{i=1,2} \frac{i}{2} \bar{N}_L^i \gamma^\mu \partial_\mu N_L^i + \sum_{i=1,2} \frac{i}{2} \bar{S}_L^i \gamma^\mu \partial_\mu S_L^i - \sum_{i,j=1,2} \mu_{ij} S_L^i S_L^j - \sum_{i,j=1,2} M_S^{ij} S_L^i N_L^j$$
$$- \sum_{i,j=1,2} M_R^{ij} N_L^i N_L^j - \sum_{i=e,\mu,\tau, j=1,2} y_{ij} \bar{L}_i \tilde{\phi}_h N_j + \text{h.c.} \quad (2.3)$$

where $\tilde{\phi}_h = i\sigma_2 \phi_h^*$. We have considered the Yukawa term for S_i to be negligible compared to the one for N_i, following the standard extended double seesaw model [8, 9]. The Yukawa terms with the dark Higgs ϕ_D are forbidden by symmetries. The parameters M_S^{ij}, M_R^{ij}, and μ_{ij} are constants with mass-dimension one, while y_{ij} are dimensionless coupling constants that compose the Dirac mass matrix M_D that we will use later. We have considered that S_L^3 and N_L^3 are decoupled from the rest of the particle spectra by assuming that they are Z_2-odd while the rest of the particles are Z_2-even. Such a discrimination ensures that the lightest particle may be treated as a FIMP-type DM candidate. Productions of S_L^3 and N_L^3 are through dimension-5 operators which get naturally suppressed when the scale of new physics Λ is large, ensuring feeble interactions with the rest of the particle spectra; in the present work, we consider $\Lambda \geq 10^{14}\,\text{GeV}$. In the neutrino sector, the effect of such dimension-5 operators is negligible. The Lagrangian associated with S_L^3 and N_L^3 is thus given by

$$\mathcal{L}_{\text{DM}} = \frac{i}{2} \bar{N}_L^3 \gamma^\mu \partial_\mu N_L^3 + \frac{i}{2} \bar{S}_L^3 \gamma^\mu \partial_\mu S_L^3 - \mu_{33} S_L^3 S_L^3 - M_S^{33} S_L^3 N_L^3 - M_R^{33} N_L^3 N_L^3$$
$$+ \frac{\kappa}{\Lambda} S_L^3 S_L^3 (\phi_h^\dagger \phi_h) + \frac{\kappa'}{\Lambda} S_L^3 S_L^3 (\phi_D^\dagger \phi_D) + \frac{\xi}{\Lambda} N_L^3 N_L^3 (\phi_h^\dagger \phi_h) + \frac{\xi'}{\Lambda} N_L^3 N_L^3 (\phi_D^\dagger \phi_D)$$
$$+ \frac{\alpha}{\Lambda} N_L^3 S_L^3 (\phi_h^\dagger \phi_h) + \frac{\alpha'}{\Lambda} N_L^3 S_L^3 (\phi_D^\dagger \phi_D) + \text{h.c.} \quad (2.4)$$

Groups &	Baryons			Leptons						Scalars	
Symmetry	$Q_L^i = (u_L^i, d_L^i)^T$	u_R^i	d_R^i	$L_L^i = (\nu_L^i, e_L^i)^T$	e_R^i	N_L^j	S_L^j	N_L^3	S_L^3	ϕ_h	ϕ_D
$\mathrm{SU}(2)_L$	2	1	1	2	1	1	1	1	1	2	1
$\mathrm{U}(1)_Y$	1/6	2/3	−1/3	−1/2	−1	0	0	0	0	1/2	0
$\mathrm{U}(1)_D$	0	0	0	0	0	0	0	0	0	0	1
Z_2	1	1	1	1	1	1	1	−1	−1	1	1

Table 1. Particle contents and their corresponding charges under different gauge groups and discrete symmetry. The index i is for three flavours, running from 1 to 3 whereas the index j runs from 1 to 2.

Finally, the term proportional to the coupling ζ denotes the gauge kinetic mixing term between the SM $\mathrm{U}(1)_Y$ gauge boson and the $\mathrm{U}(1)_D$ gauge boson. It has been shown that small values of the parameter ζ are favoured from the viewpoint of the muon $g-2$ [122, 123]; see also, e.g., ref. [124] for various experimental constraints on ζ. In this work, we shall ignore the gauge kinetic mixing term to ensure that the $\mathrm{U}(1)_D$ gauge boson W_D becomes a stable WIMP DM candidate. One may alternatively impose an upper bound of $\zeta \lesssim 10^{-20}$ by requiring that the lifetime of W_D is larger than the age of the Universe; see appendix A for details.[2] Additionally, to consider W_D as the WIMP DM, which is one of the main motivations of the present work, we consider all the particles to be neutral in $\mathrm{U}(1)_D$ except the singlet scalar ϕ_D which is necessary for obtaining the W_D mass. Introduction of $\mathrm{U}(1)_D$ charges to any other fields would make W_D unstable. Table 1 summarises the particle contents of the model under consideration and their charges.

The presence of an extra scalar that interact with the ϕ_h induces a mixing between the two. In unitary gauge, the expressions of ϕ_h and ϕ_D, after the spontaneous breaking of the gauge symmetry, are given by

$$\phi_h = \begin{pmatrix} 0 \\ \dfrac{v + H}{\sqrt{2}} \end{pmatrix}, \qquad \phi_D = \frac{v_D + H_D}{\sqrt{2}}, \tag{2.5}$$

with the mass matrix

$$\mathcal{M}_{\mathrm{scalar}}^2 = \begin{pmatrix} 2\lambda_h v^2 & \lambda_{hD} v_D v \\ \lambda_{hD} v_D v & 2\lambda_D v_D^2 \end{pmatrix}. \tag{2.6}$$

Here, v (v_D) denotes the VEV of the SM (dark) Higgs ϕ_h (ϕ_D). Diagonalisation of the mass matrix leads to the mass eigenstates

$$\begin{aligned} H_1 &= H \cos\theta - H_D \sin\theta, \\ H_2 &= H \sin\theta + H_D \cos\theta, \end{aligned} \tag{2.7}$$

---

[2]In fact, a stronger bound, $\zeta \lesssim 10^{-26}$, exists when we take into account γ-ray observation [125].

where θ is the mixing angle, given by

$$\tan 2\theta = \frac{\lambda_{hD}\, v_D\, v}{\lambda_h v^2 - \lambda_D v_D^2}\,. \tag{2.8}$$

The mass eigenvalues are

$$M_{H_1}^2 = \lambda_h v^2 + \lambda_D v_D^2 + \sqrt{(\lambda_h v^2 - \lambda_D v_D^2)^2 + (\lambda_{hD}\, v\, v_D)^2}\,,$$
$$M_{H_2}^2 = \lambda_h v^2 + \lambda_D v_D^2 - \sqrt{(\lambda_h v^2 - \lambda_D v_D^2)^2 + (\lambda_{hD}\, v\, v_D)^2}\,. \tag{2.9}$$

We consider the case where the dark Higgs is lighter than the SM Higgs. In other words, M_{H_2} denotes the mass of the dark Higgs, and M_{H_1} matches the SM Higgs mass. One may express the scalar quartic couplings in terms of the mixing angle and masses of the physical Higgses; we present the expressions in appendix B. When the dark Higgs acquires a VEV, the $U(1)_D$ gauge boson W_D gets the mass of $M_{W_D} = g_D v_D$.

2.1 Generation of neutrino masses with the extended seesaw mechanism

We consider the first two generations of the additional fermions, namely N_L^1, N_L^2, S_L^1, and S_L^2, to take part in the neutrino mass generation. The third generation is decoupled from the visible sector which is achieved by making them Z_2-odd. Therefore, the neutrino mass matrix can be expressed as

$$\mathcal{L}_{NM} = -\frac{1}{2}\begin{pmatrix} \nu_L & S_L & N_L \end{pmatrix}\begin{pmatrix} 0 & 0 & M_D^T \\ 0 & \mu & M_S^T \\ M_D & M_S & M_R \end{pmatrix}\begin{pmatrix} \nu_L \\ S_L \\ N_L \end{pmatrix} + \text{h.c.} \tag{2.10}$$

Here, M_D is the 2×3 Dirac mass matrix,

$$M_D = \begin{pmatrix} m_D^{e1} & m_D^{\mu1} & m_D^{\tau1} \\ m_D^{e2\,R} + im_D^{e2\,I} & m_D^{\mu2\,R} + im_D^{\mu2\,I} & m_D^{\tau2\,R} + im_D^{\tau2\,I} \end{pmatrix}, \tag{2.11}$$

where $m_D^{ij} = y_{ij} v/\sqrt{2}$ and the superscript R (I) stands for the real (imaginary) part. On the other hand, M_R and M_S in eq. (2.10) are 2×2 matrices which we choose to take as follows:

$$M_R = \begin{pmatrix} M_R^{11} & 0 \\ 0 & M_R^{22} \end{pmatrix}, \qquad M_S = \begin{pmatrix} M_S^{11} & 0 \\ 0 & M_S^{22} \end{pmatrix}. \tag{2.12}$$

Finally, we choose μ as a symmetric matrix. It is in general complex, and we parametrise it as

$$\mu = \begin{pmatrix} \mu_{11}^R + i\mu_{11}^I & \mu_{12}^R + i\mu_{12}^I \\ \mu_{12}^R + i\mu_{12}^I & \mu_{22}^R + i\mu_{22}^I \end{pmatrix}. \tag{2.13}$$

To realise the non-zero neutrino masses in the extended seesaw framework, we consider the following hierarchy amongst the elements of M_D, M_R, and M_S mass matrices [9]:

$$M_R > M_S > M_D \gg \mu\,, \qquad \mu < M_S^T M_R^{-1} M_S\,. \tag{2.14}$$

With these assumptions, we can diagonalise the mass matrix shown in eq. (2.10) and obtain the following set of mass matrices [9]:

$$
\begin{aligned}
m_\nu &\simeq M_D^T (M_S^T)^{-1} \mu M_S^{-1} M_D \,, \\
m_S &\simeq -M_S^T M_R^{-1} M_S \,, \\
m_N &\simeq M_R \,.
\end{aligned}
\tag{2.15}
$$

Once we diagonalise the 3×3 matrix m_ν, we get the masses of the active neutrinos. The other two matrices give the masses of the sterile neutrinos. After the diagonalisation, we find the relation between the flavour basis $(\nu_L \; S_L \; N_L)^T$ and mass basis $(\nu_m \; S_m \; N_m)^T$ as

$$
\begin{pmatrix} \nu_L^i \\ S_L^i \\ N_L^i \end{pmatrix} = \mathcal{U} \begin{pmatrix} \nu_m^i \\ S_m^i \\ N_m^i \end{pmatrix} \,,
\tag{2.16}
$$

where the matrix $\mathcal{U} = \mathcal{U}_1 \mathcal{U}_2$. Note that $\mathcal{U}_1$ diagonalises the matrix in eq. (2.10), while $\mathcal{U}_2$ diagonalises the mass matrices given in eq. (2.15). The expressions of $\mathcal{U}_1$ and $\mathcal{U}_2$ are given by [9]

$$
\mathcal{U}_1 = \begin{pmatrix} 1 - \frac{1}{2} M_D^\dagger (M_S^{-1})^\dagger M_S^{-1} M_D & M_D^\dagger (M_S^{-1})^\dagger & M_D^\dagger M_R^{-1} \\ -M_S^{-1} M_D & 1 - \frac{1}{2}(M_S^{-1} M_D)(M_S^{-1} M_D)^\dagger - \frac{1}{2} M_S^\dagger M_R^{-2} M_S & M_S^\dagger M_R^{-1} \\ (M^T)_S^{-1} \mu M_S^{-1} M_D & -M_R^{-1} M_S & 1 - \frac{1}{2} M_R^{-1} M_S M_S^\dagger M_R^{-1} \end{pmatrix} \,,
\tag{2.17}
$$

and

$$
\mathcal{U}_2 = \begin{pmatrix} U & 0 & 0 \\ 0 & W_S & 0 \\ 0 & 0 & W_N \end{pmatrix} \,,
\tag{2.18}
$$

where U, which is the Pontecorvo-Maki-Nakagawa-Sakata (PMNS) matrix [126, 127], W_S, and W_N diagonalise m_ν, m_S, and m_N, respectively [9].

2.2 FIMP dark matter candidate

The remaining singlet neutrinos, N_L^3 and S_L^3, comprise a 2×2 mass matrix, and the lighter one is a good DM candidate. The mass matrix for the DM sector takes the following form:

$$
\mathcal{L}_{\mathrm{FIMP}} = \begin{pmatrix} S_L^3 & N_L^3 \end{pmatrix} \begin{pmatrix} \mu'_{33} & M'^{33}_{SN} \\ M'^{33}_{SN} & M'^{33}_R \end{pmatrix} \begin{pmatrix} S_L^3 \\ N_L^3 \end{pmatrix} \,,
\tag{2.19}
$$

where the elements are given by

$$
\begin{aligned}
\mu'_{33} &= \mu_{33} + \frac{\kappa v^2}{2\Lambda} + \frac{\kappa' v_D^2}{2\Lambda} \,, \\
M'^{33}_{SN} &= M_S^{33} + \frac{\alpha v^2}{2\Lambda} + \frac{\alpha' v_D^2}{2\Lambda} \,, \\
M'^{33}_R &= M_R^{33} + \frac{\xi v^2}{2\Lambda} + \frac{\xi' v_D^2}{2\Lambda} \,.
\end{aligned}
\tag{2.20}
$$

In the limit $M_R'^{33} \gg M_{SN}'^{33}$, we diagonalise the mass matrix to obtain the eigenvalues expressed as

$$M_{S_m} = \mu'_{33} - \frac{(M_{SN}'^{33})^2}{M_R'^{33}},$$
$$M_{N_m} = M_R'^{33}. \tag{2.21}$$

The relation between the mass eigenstates and the flavour eigenstates are given by

$$\begin{pmatrix} S_m^3 \\ N_m^3 \end{pmatrix} \simeq \begin{pmatrix} 1 & \frac{M_{SN}'^{33}}{M_R'^{33}} \\ -\frac{M_{SN}'^{33}}{M_R'^{33}} & 1 \end{pmatrix} \begin{pmatrix} S_L^3 \\ N_L^3 \end{pmatrix} = \begin{pmatrix} 1 & \delta \\ -\delta & 1 \end{pmatrix} \begin{pmatrix} S_L^3 \\ N_L^3 \end{pmatrix}, \tag{2.22}$$

where $\delta \equiv M_{SN}'^{33}/M_R'^{33}$. In our study, S_m^3 is the lighter one, becoming a good DM candidate, and N_m^3 is the next-to-lightest stable particle (NLSP). We shall drop the superscript '3' and use S_m and N_m to denote the lighter third-generation mass eigenstate, which becomes the FIMP DM, and the heavier third-generation mass eigenstate, which is the NLSP, respectively, hereinafter.

In section 4, we shall explore the DM phenomenology in detail, focusing on the parameter space where $\Lambda \gtrsim 10^{14}$ GeV and $\alpha = \alpha' = \xi = \xi' = \kappa = \kappa' = \mathcal{O}(1)$. In this case, both the DM candidate S_m and the NLSP N_m are produced out-of-equilibrium in the early Universe through the freeze-in processes of the type $H_i(+H_i) \to \text{FIMP} + \text{FIMP}$, where $i = 1, 2$. Thus, the effective couplings are in the ballpark of the FIMP-type DM. After the production, the NLSP decays into the lighter eigenstate; see section 4 for details.

2.3 WIMP dark matter candidate

The vector gauge boson W_D associated with the extra dark $\text{U}(1)_D$ is, on the other hand, a good WIMP DM candidate in our model. The vector boson W_D, being a WIMP, is produced via the standard freeze-out processes $\text{SM} + \text{SM} \leftrightarrow W_D + W_D$ which keep the WIMP in thermal equilibrium with the SM thermal bath.

As the model features both the FIMP DM, S_m, and the WIMP DM, W_D, a two-component DM scenario naturally arises in our model. We will present the detailed analysis in section 4.

3 Neutrino masses and lepton flavour violation bounds

The eigenvalues of the mass matrix m_ν represent the masses of the active neutrinos as we discussed in section 2.1. Differences of their mass-squared will give us the solar mass difference Δm_{12}^2 and the atmospheric mass difference Δm_{31}^2. On the other hand, the elements of the PMNS matrix U give us the oscillation angles θ_{12}, θ_{13}, and θ_{23}. In this work, we consider the recent bounds on the oscillation parameters [3],

$$6.82 \leq \frac{\Delta m_{21}^2}{10^{-5} \text{ eV}^2} \leq 8.04, \qquad 2.431 \leq \frac{\Delta m_{31}^2}{10^{-3} \text{ eV}^2} \leq 2.599,$$

$$31.27 \leq \theta_{12} \, [^0] \leq 35.86, \qquad 8.20 \leq \theta_{13} \, [^0] \leq 8.97, \qquad 39.5 \leq \theta_{23} \, [^0] \leq 52.00. \tag{3.1}$$

Additionally, we consider the bound on the sum of the non-decaying active neutrino masses from cosmology, i.e., $\sum_i m_{\nu_i} < 0.23\,\text{eV}$ [4, 5]. Since we have additional sterile neutrinos, we also take into account the LFV processes. The most stringent bounds on the LFV processes come from $\mu \to e\gamma$, $\mu \to eee$, and μ-to-e conversion CR$(\mu^- \text{Ti} \to e^- \text{Ti})$. The recent bounds are given by Br$(\mu \to e\gamma) < 4.2 \times 10^{-13}$ [128], Br$(\mu \to e\bar{e}e) < 1 \times 10^{-12}$ [129], and CR$(\mu^- \text{Ti} \to e^- \text{Ti}) < 6.1 \times 10^{-13}$ [130]. In determining the branching ratios for $\mu \to e\gamma$, $\mu \to e\bar{e}e$, and $\mu - e$ conversion rate, we follow refs. [131, 132]. In order to satisfy all the aforementioned constraints, the elements shown in eq. (2.11) and eq. (2.12) cannot take arbitrary values. We thus vary the model parameters as below and obtain allowed parameter spaces by imposing the aforementioned constraints:

$$1 \leq M_S^{11} (= M_S^{22})\,[\text{GeV}] \leq 1000\,, \quad 10^{-5} \leq \frac{m_D^{\alpha 1}}{M_S^{11}}\,, \quad \frac{m_D^{\alpha 2\,R,I}}{M_S^{11}} \leq 10^{-1}\,,$$

$$10^{-9} \leq \mu_{ij}^{R,I}\,[\text{GeV}] \leq 10^{-1}\,, \tag{3.2}$$

where $\alpha = \{e, \mu, \tau\}$ and $i, j = 1, 2$, and we have chosen $M_{N^1} = M_{N^2} = 2M_S^{11}$. The rest of the model parameters, which affect the DM relic density directly but do not take part in the neutrino mass, are fixed as

$$M_{S_m} = 20\,\text{GeV}\,, \quad M_{W_D} = 1.04628\,\text{GeV}\,, \quad M_{N_m} = 300\,\text{GeV}\,, \quad M_{H_2} = 2.2120\,\text{GeV}\,,$$

$$g_D = 3.1 \times 10^{-4}\,, \quad \sin\theta = 8.17 \times 10^{-2}\,, \quad \Lambda = 5.5 \times 10^{14}\,\text{GeV}\,,$$

$$\kappa = \kappa' = \alpha = \alpha' = \xi = \xi' = 1\,. \tag{3.3}$$

These fixed values are inspired by the DM studies as well as the FOPTs, as we will discuss later in the paper.

In the left panel (LP) and right panel (RP) of figure 1, allowed parameter spaces are shown in the $m_D^{e1} - m_D^{\mu 1}$ and $\mu_{11}^R - m_D^{e1}$ planes, respectively. The cyan points are obtained after imposing the NOD constraints. The blue points are obtained when we additionally impose the LFV bounds. From the LP of figure 1, one may see a sharp correlation between m_D^{e1} and $m_D^{\mu 1}$. This is because both of them actively contribute to the neutrino mass, i.e., they are the leading contributions in two different elements of the neutrino mass matrix m_ν. Since we have taken the elements of M_S to be equal, for a large value of M_S, we need a small value for m_D^{e1} and $m_D^{\mu 1}$, and similarly, for a small value of M_S, we need a large value for m_D^{e1} and $m_D^{\mu 1}$. Moreover, the LFV processes are mediated by the gauge bosons ($W^\pm, Z$), so those processes mainly depend on the active-sterile mixing terms, namely M_D/M_S and M_D/M_R. Therefore, when we apply the LFV bounds, higher values of $m_D^{\mu 1}$ get ruled out for each value of m_D^{e1}. On the other hand, in the RP of figure 1, we see an anti-correlation between m_D^{e1} and μ_{11}^R, which is mainly due to the neutrino mass relation. Furthermore, elements of the matrix μ do not actively contribute to the LFV processes. Therefore, there is practically no shrink in the $\mu_{11}^R - m_D^{e1}$ plane after applying the LFV bounds.

In figure 2, we have shown the allowed parameter space in the $m_D^{e1}/M_S^{11} - m_D^{\tau 1}/M_S^{11}$ and $m_D^{e2\,R}/M_S^{11} - m_D^{\mu 2\,R}/M_S^{11}$ planes in the LP and RP, respectively, after imposing the NOD (cyan) and NOD plus LFV bounds (blue). The LFV bounds directly depend on the parameters $m_D^{\tau 1}/M_S^{11}$, $m_D^{\tau 1}/M_S^{11}$, $m_D^{e2\,R}/M_S^{11}$, and $m_D^{\mu 2\,R}/M_S^{11}$ as they represent the strength
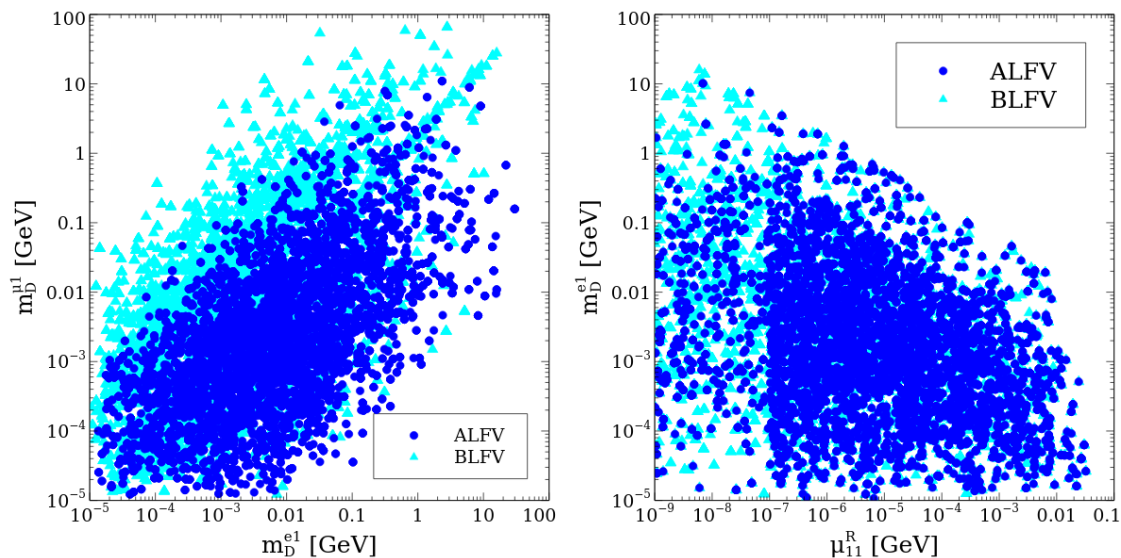
Figure 1. Allowed parameter spaces after imposing the NOD constraints (cyan) and the NOD constraints plus LFV bounds (blue) are shown in the $m_D^{e1} - m_D^{\mu1}$ plane in the left panel and in the $\mu_{11}^R - m_D^{e1}$ plane in the right panel. ALFV and BLFV respectively correspond to after and before imposing the LFV bounds.
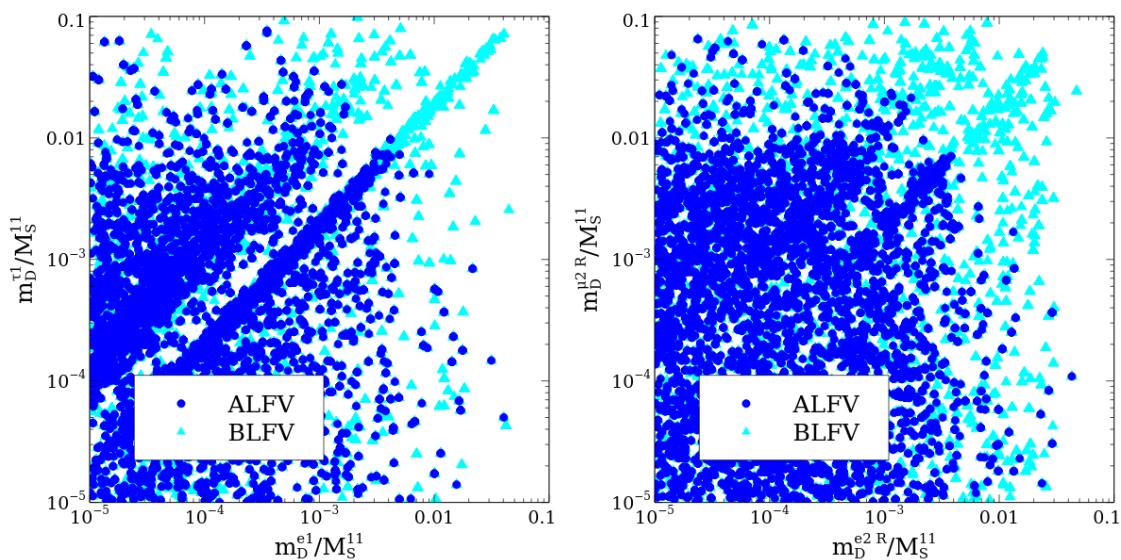

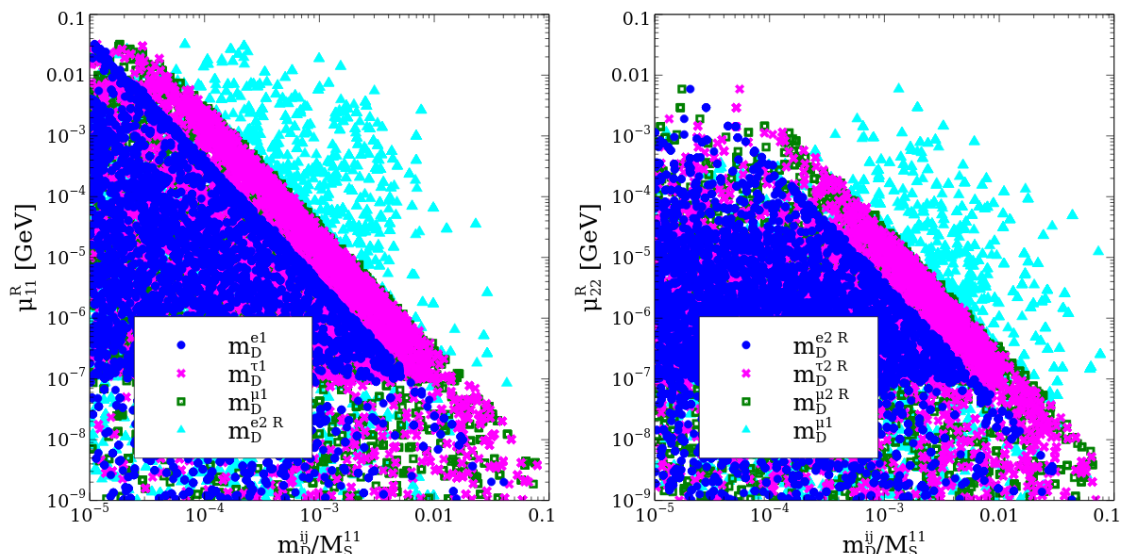**Figure 2**. Allowed parameter spaces after imposing the NOD constraints (cyan) and the NOD constraints plus LFV bounds (blue) are shown in the $m_D^{e1}/M_S^{11} - m_D^{\tau1}/M_S^{11}$ plane in the left panel and in the $m_D^{e2\,R}/M_S^{11} - m_D^{\mu2\,R}/M_S^{11}$ plane in the right panel. ALFV and BLFV respectively correspond to after and before imposing the LFV bounds.

Figure 3. Allowed parameter spaces after imposing the NOD constraints and the LFV bounds are shown in the $m_D^{ij}/M_S^{11} - \mu_{11}^R$ ($ij = \{e1, \tau1, \mu1, e2\,R\}$) plane in the left panel and in the $m_D^{ij}/M_S^{11} - \mu_{22}^R$ ($ij = \{e2\,R, \tau2\,R, \mu2\,R, \mu1\}$) plane in the right panel.

of the active-sterile mixing. Therefore, in the LP of figure 2, we see that both parameters cannot take higher values simultaneously due to the LFV bounds. The same conclusion is also observed for the RP. Depending on the strength of the active-sterile mixing, we may detect the sterile neutrinos in many ongoing and future experiments which we shall discuss later in figure 4 and figure 5.

In figure 3, we have shown the scatter plots in the $M_D/M_S - \mu$ plane after imposing the NOD and LFV bounds. In the LP of figure 3, blue, magenta, green, and cyan points respectively correspond to $m_D^{e1}/M_S^{11} - \mu_{11}^R$, $m_D^{\tau1}/M_S^{11} - \mu_{11}^R$, $m_D^{\mu1}/M_S^{11} - \mu_{11}^R$, and $m_D^{e2\,R}/M_S^{11} - \mu_{11}^R$. In the RP, we have blue, magenta, green, and cyan points for $m_D^{e2\,R}/M_S^{11} - \mu_{22}^R$, $m_D^{\tau2\,R}/M_S^{11} - \mu_{22}^R$, $m_D^{\mu2\,R}/M_S^{11} - \mu_{22}^R$, and $m_D^{\mu1}/M_S^{11} - \mu_{22}^R$, respectively. One interesting point to note here is that there is a strong correlation amongst the blue, magenta, and green points in both the LP and RP, while we observe no relation amongst the cyan points. The points that exhibit the strong correlation strictly follow the relation $(M_D/M_S)^2\mu < 10^{-11}\,\text{GeV}$, which is the mass of the active neutrinos. Parameters denoted by the cyan points do not affect the neutrino mass directly; they either come with the multiplication of other terms or are absent in the neutrino mass matrix. Thus, in the end, their combinational effect never exceeds the light active neutrino mass.

In the LP of figure 4, we have shown the allowed parameter space in terms of the Yukawa coupling y_{e1} and the DM relic density that is coming solely from the neutrino sector. S_m, which is a FIMP DM candidate as we discussed in section 2, may be produced via annihilations of active neutrinos and extra heavy neutrinos, mediated by the Higgses, as $\nu_i + N_j \xrightarrow{H_{1,2}} S_m + S_m$ and $\nu_i + S_j \xrightarrow{H_{1,2}} S_m + S_m$, where $i = 1, 2, 3$ and $j = 1, 2$. The LP of figure 4 indicates that this contribution is subdominant. One may understand the general behaviour as follows. When M_{N_1} is smaller than $500\,\text{GeV}$, we have a linear relation between
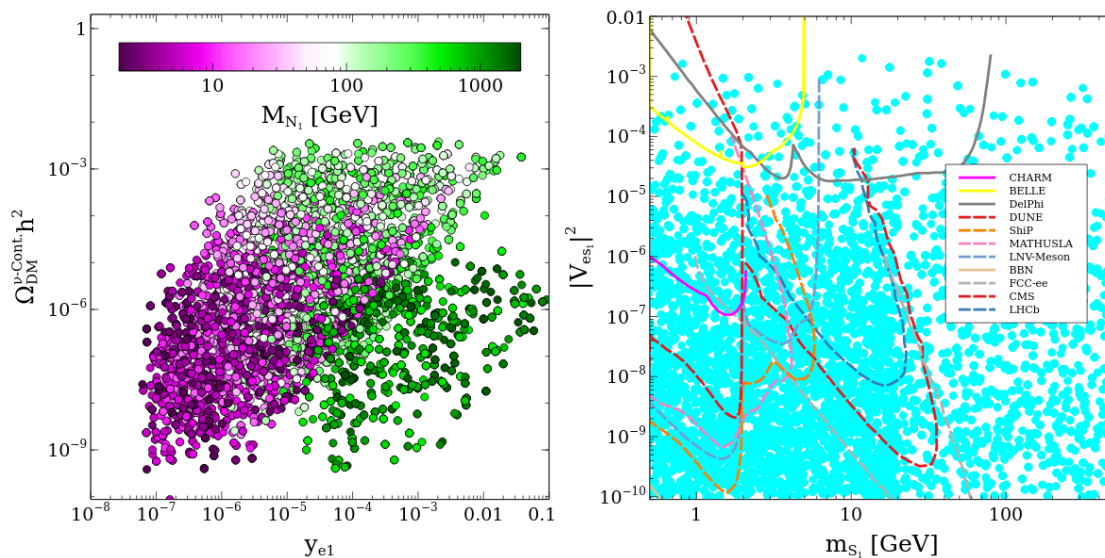
Figure 4. Allowed parameter spaces in the $y_{e1} - \Omega_{\text{DM}}^{\nu-\text{Cont.}} h^2$ (left) and $m_{S_1} - |V_{eS_1}|^2$ (right) planes after imposing the NOD constraints. Bounds coming from various ongoing (solid lines) and future (dashed lines) experiments are overlaid; see text for more details.
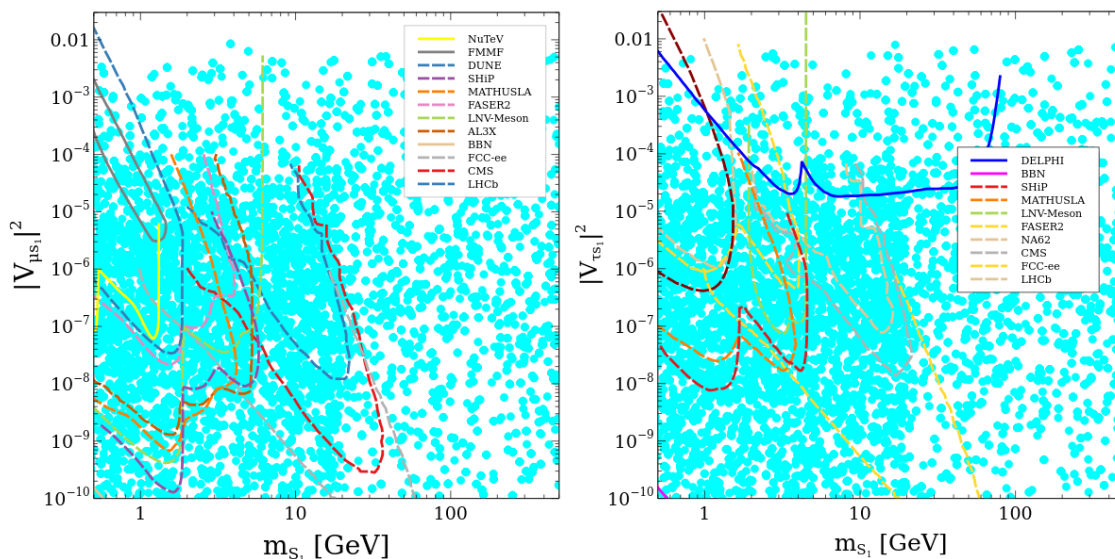

Figure 5. Allowed parameter spaces in the $m_{S_1} - |V_{\mu S_1}|^2$ (left) and $m_{S_1} - |V_{\tau S_1}|^2$ (right) planes after imposing the NOD constraints. Bounds coming from various ongoing (solid lines) and future (dashed lines) experiments are overlaid; see text for more details.

y_{e1} and the DM relic density coming from the active and heavy neutrinos annihilations. It reflects the fact that $\Omega_{\rm DM}^{\nu-{\rm Cont.}} h^2 \propto y_{e1}^2$. When M_{N_1} is larger than $1000\,{\rm GeV}$, the contribution to the DM relic density is small as the mass is close to the chosen reheating temperature of $T_R = 3\,{\rm TeV}$; thus, a suppression occurs. We observe that, for the chosen range of parameter values (3.2), the contribution of the active and extra heavy neutrinos to the total DM relic density is at most $\sim 3\%$. The RP of figure 4 depicts the allowed region in the active-sterile mixing angle associated with electron $|V_{eS_1}|^2$ and sterile neutrino mass m_{S_1} plane after imposing the NOD bounds. The solid lines represent the present bounds which come from CHARM [133, 134], BELLE [135], and DelPhi [136], depending on the mass of the sterile neutrino. DelPhi demands the allowed range $|V_{eS_1}|^2 < 10^{-4}$ for the sterile neutrino mass up to $100\,{\rm GeV}$, whereas CHARM puts a bound on the active-sterile mixing angle $|V_{eS_1}|^2 \lesssim 10^{-7}$ for the sterile neutrino mass less than $2\,{\rm GeV}$. There are various proposed experiments, including DUNE [137, 138], SHiP [139], MATHUSLA [140], LNV-Meson [141], FCC-ee [142, 143], CMS [144], and LHCb [144, 145], which have the sensitivity reaching up to $|V_{eS_1}|^2 \sim 10^{-10}$ for the sterile neutrino mass up to $100\,{\rm GeV}$.

Figure 5 shows the allowed region in the active-sterile mixing associated with the muon $|V_{\mu S_1}|^2$ (LP) as well as tauon $|V_{\tau S_1}|^2$ (RP) and the sterile neutrino mass m_{S_1} planes, after imposing the NOD bounds. In the LP, the recent bounds put by NuTeV [146] and FMMF [147] already rule out the sterile neutrino mass up to $2\,{\rm GeV}$ for the active-sterile neutrino mixing larger than 10^{-7}. Various future experiments such as DUNE [137, 138], SHiP [139], MATHUSLA [140], FASER2 [148], LNV-Meson [141], AL3X [149], FCC-ee [142, 143], CMS [144], and LHCb [144, 145] are also presented by dashed lines which will probe the active-sterile mixing, $|V_{\mu S_1}|^2$, up to 10^{-10} for sterile neutrino mass as large as $100\,{\rm GeV}$. On the other hand, from the RP of figure 5, we see that the DELPHI experiment [136] already rules out $|V_{\tau S_1}|^2 > 3 \times 10^{-5}$ for the sterile neutrino mass up to $100\,{\rm GeV}$. The future experiments shall cover the active-sterile mixing up to $|V_{\tau S_1}|^2 \sim 10^{-10}$ for the mass range up to $100\,{\rm GeV}$. For all the active-sterile mixing and sterile neutrino mass planes, there exits a bound coming from the Big Bang Nucleosynthesis (BBN) as well, if the sterile neutrino decays after the BBN. However, the BBN bound is weak for the parameter space we have considered.

4 Dark matter phenomenology

We now discuss the production and detection prospects of the DM candidates in our model.[3] Our model features both the WIMP and FIMP DM candidates as we discussed in section 2. The dark gauge boson W_D plays the WIMP role, and the lighter singlet neutrino of the third generation S_m becomes the FIMP DM; the NLSP, N_m, will eventually decay to the FIMP DM S_m. Thus, a two-component DM scenario naturally arises. The WIMP part ensures the potential detectability in future, whereas the FIMP DM will be difficult to probe by the direct, indirect, or collider detection techniques.

---

[3]We have utilised publicly available tools, including `FeynRules` [150], `CalcHEP` [151], and `microMEGAs` [152], for the DM studies.
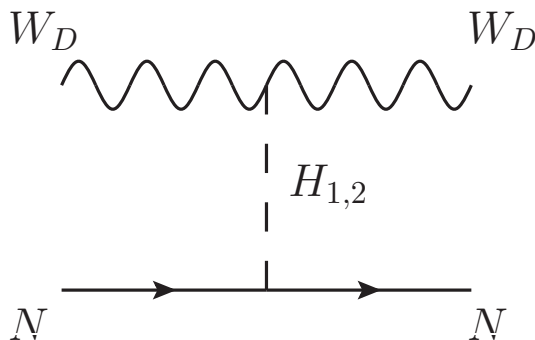
Figure 6. DM direct detection diagram mediated by $H_{1,2}$.

As we shall discuss in section 5, a low-mass BSM dark Higgs is favoured from the FOPT point of view [153]. Thus, in this section, we mainly focus on the range $1 - 200\,\text{GeV}$ for the dark Higgs. Furthermore, to avoid any potential problems with collider searches due to the low mass of the dark Higgs, we consider the mixing angle θ in eq. (2.8) to be small, focusing on $|\sin\theta| < 0.1$. In doing so, we may easily evade the Higgs signal strength bounds [154, 155].

There are mainly five constraints that we have taken into account for the discussion of DM phenomenology: *i)* relic density, *ii)* direct detection bounds, *iii)* indirect detection bounds, *iv)* Higgs invisible decay, and *v)* Higgs signal strength bound. We explain each category below before presenting the results.

- **DM relic density.** We consider the bound on the total amount of DM relic density coming from the Planck experiment [4, 5]. Specifically, the following 3σ bound is used, unless stated otherwise:

$$0.1172 \leq \Omega_{\text{DM}} h^2 (= \Omega_{W_D} h^2 + \Omega_{S_m} h^2) \leq 0.1226 \,. \tag{4.1}$$

  Here, $\Omega_{W_D} h^2$ $(\Omega_{S_m} h^2)$ denotes the WIMP (FIMP) DM relic density.

- **Direct detection.** In our model, DM can have the elastic scattering with a nucleon N as depicted in figure 6. The analytical estimate for such a process takes the form [156],

$$\sigma_{\text{SI}} = \frac{\mu_*^2 \sin^2 2\theta\, g_D^2}{4\pi v^2} \left(\frac{1}{M_{H_1}^2} - \frac{1}{M_{H_2}^2}\right)^2 \left[\frac{Z\tilde{f}_p + (A-Z)\tilde{f}_n}{A}\right]^2 \,, \tag{4.2}$$

  where $\mu_* = M_{W_D} M_N / (M_{W_D} + M_N)$ is the reduced mass, with M_N being the nucleon mass, v is the electroweak VEV, Z is the atomic number, A is the atomic weight, and $\tilde{f}_\alpha$ $(\alpha = p, n)$ can be expressed as

$$\frac{f_\alpha}{M_N} = \left(\frac{7}{9} \sum_{q=u,d,s} f_{T_q}^\alpha + \frac{2}{9}\right) \,, \tag{4.3}$$

– 14 –

with $f_{T_u}^{p(n)} = 0.020(0.026)$, $f_{T_d}^{p(n)} = 0.026(0.020)$, and $f_{T_s}^{p,n} = 0.043$ [157]. As we take the WIMP DM mass to be in the range of $1 - 100\,\text{GeV}$, the DM may be detected by different experiments. A part of the parameter space in the spin-independent direct detection (SIDD) cross-section, σ_{SI}, and DM mass, M_{W_D}, plane is already ruled out by LUX-ZEPLIN-5.5T [158], PandaX-4T [159, 160], and Xenon-1T [19] for the $10 - 100\,\text{GeV}$ DM mass range. On the other hand, the mass range below $10\,\text{GeV}$ will be explored by experiments such as DarkSide-50 [161, 162], XENON-1T (M) [163], CDMSlite [164], and CRESST-III [165, 166]. Our SIDD cross-section is a few orders of magnitude below the current bound.

- **Indirect Detection.** The WIMP DM can also be detected by observing the annihilation products, namely $b\bar{b}$, $\tau\bar{\tau}$, $\mu\bar{\mu}$, and $e\bar{e}$. When the WIMP DM mass is above the b-quark mass, the bound from the $b\bar{b}$ final state dominates. Fermi-LAT + MAGIC Segue 1 [21] puts the stringent bound on the $\langle\sigma v\rangle_{b\bar{b}} - M_{W_D}$ plane. On the other hand, when the DM mass is smaller than the b-quark mass, the DM annihilates to $\tau\bar{\tau}$, $\mu\bar{\mu}$, and $e\bar{e}$ dominantly. The bounds come from the study of FERMI-LAT [167, 168], CMB [168], and AMS [168, 169]. We shall discuss the details of the indirect detection bound when we present our resultant plots.

- **Invisible decay.** When the DM mass is below half of the SM Higgs mass, there is a possibility that the SM Higgs will have an invisible decay, $\Gamma_{H_1}^{\text{inv}}$. Thus, one needs to make sure that the invisible decay is always smaller than the current bound [170],

$$\frac{\Gamma_{H_1}^{\text{inv}}}{\Gamma_{H_1}} < 0.26 \,. \tag{4.4}$$

The decay width of the SM Higgs to the WIMP DM in the present case takes the form,

$$\Gamma_{H_1}^{\text{inv}} = \frac{M_{H_1}^3 g_{H_1 W_D W_D}^2}{128\,\pi M_{W_D}^4} \sqrt{1 - \frac{4M_{W_D}^2}{M_{H_1}^2}} \left(1 - \frac{4M_{W_D}^2}{M_{H_1}^2} + \frac{12M_{W_D}^4}{M_{H_1}^4}\right) , \tag{4.5}$$

where $g_{H_1 W_D W_D} = -2g_D M_{W_D} \sin\theta$. The allowed parameter region in the $M_{W_D} - \sigma_{\text{SI}}$ plane after imposing the invisible decay constraints shall be presented in section 4.2 with the SM Higgs decay width $\Gamma_{H_1} = 4.156\,\text{MeV}$.

- **Higgs signal strength.** The Higgs signal strength can be estimated by measuring its production and decay ratio with the SM values. It can be defined as

$$\tilde{\mu} = \mu_{H_1}\mu_f = \frac{\sigma_{H_1}}{\sigma_{H_1}^{\text{SM}}} \frac{\mathcal{B}_f}{\mathcal{B}_f^{\text{SM}}} \,, \tag{4.6}$$

where $\mu_{H_1} = \sigma_{H_1}/\sigma_{H_1}^{\text{SM}}$ is the ratio of the Higgs production in the new model and the SM, and $\mu_f = \mathcal{B}_f/\mathcal{B}_f^{\text{SM}}$ is the ratio of the branchings of the Higgs to a channel f. The current bound on $\tilde{\mu}$ after a combined analysis is given by [154]

$$\tilde{\mu} = 1.17 \pm 0.10 \,. \tag{4.7}$$

Assuming that the Higgs boson has the same kind of branchings as the SM case, we find that $\tilde{\mu} \sim \cos^2 \theta$. By taking the 3σ range, we obtain that $\sin \theta < 0.36$. Since we consider a small mixing angle, namely $\sin \theta < 0.1$, we thus always satisfy the bound from the Higgs signal strength.

4.1 Dark matter production

Let us temporarily consider a regime where only the coupling κ is active and the mixing between S_L^3 and N_L^3 is negligible, in which case $S_m \simeq S_L^3$. Let us also consider the case where the mixing between the Higgses is small, i.e., $\cos \theta \simeq 1$. In this case, the FIMP DM S_m is produced dominantly by the Higgs scattering process, and the analytical solution for the yield is given by [28]

$$Y_{S_m} = \int_{T_{\rm end}}^{T_R} \frac{1}{S \mathcal{H} T} \left(\frac{4\kappa}{\Lambda} \right)^2 \frac{1}{16\pi^5} \, {\rm T}^6 \,, \tag{4.8}$$

where T_R is the reheating temperature, $T_{\rm end} \simeq 1\,{\rm MeV}$ is the temperature after which we may safely assume that no DM production occurs, and the entropy S and the Hubble parameter $\mathcal{H}$ are given by

$$S = \frac{2\pi^2 g_S T^3}{45} \,, \qquad \mathcal{H} = \frac{1.66\sqrt{g_\rho} T^2}{M_{\rm Pl}} \,, \tag{4.9}$$

with $M_{\rm Pl} = 1.22 \times 10^{19}\,{\rm GeV}$, and g_S and g_ρ being respectively the entropy and the energy density degrees of freedom of the Universe; we take $g_{S,\rho} \sim 100$. In achieving eq. (4.8), it is assumed that the masses of the associated particles in the production may be neglected compared to the temperature at which DM production happens which, for the process under consideration, is the reheating temperature. Thus, the production depends on the highest temperature, obtaining the UV freeze-in contribution. Consideration of masses of the associated particles has therefore a negligible effect in the DM production. Moreover, as in the IR freeze-in case, it is assumed that one may safely ignore the back-reaction of the DM in the Boltzmann equations since the number density is always smaller than the equilibrium number density. With these assumptions, the final relic density for the T_R-dominated regime is given by

$$\Omega_{S_m} h^2 = M_{S_m} \frac{S_0}{\rho_c} Y_{S_m} \,, \tag{4.10}$$

where $S_0/\rho_c \simeq 2.74 \times 10^8$ is the ratio of the entropy today and the critical energy density. We have checked that the result from numerical analyses performed by using micrOMEGAs [152] for the T_R-dominated regime matches well with the analytical expression (4.8). Figure 7 shows the relic density of the FIMP DM, $\Omega_{S_m} h^2$, in the $T_R - \Lambda$ plane, using the analytical result. The black dashed line indicates the correct relic abundance. We see that low values of the reheating temperature are preferred. For the rest of the work, we will therefore concentrate on the low reheating temperature. In particular, we shall choose $T_R = 3\,{\rm TeV}$ throughout this section.
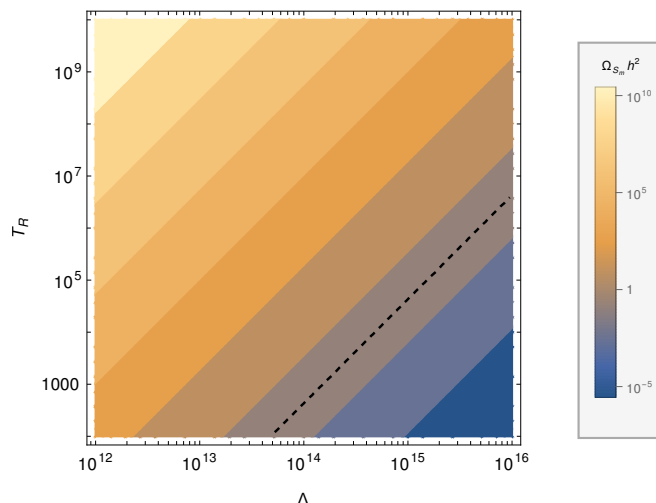
Figure 7. FIMP DM relic density in terms of Λ and the reheating temperature T_R in units of GeV. The black dashed line indicates the correct relic abundance. Here, $M_{S_m} = 100\,\text{GeV}$ is chosen. One may notice that low values of T_R are preferred to obtain a correct relic abundance.

With the knowledge obtained above, we now re-introduce all the couplings and numerically evolve the full Boltzmann equations using `microOMEGAs` to obtain the DM relic densities. The relevant Boltzmann equations are

$$\frac{dY_{W_D}}{dz} = -\frac{2\pi^2}{45}\frac{M_{\text{Pl}}M_{H_1}\sqrt{g_\rho(z)}}{1.66z^2}\sum_{A,B\in\text{SM}}\langle\sigma v\rangle_{W_D W_D\to AB}\left(Y_{W_D}^2 - Y_{W_D}^{\text{eq}\,2}\right)$$

$$\frac{dY_{N_m}}{dz} = \frac{4\pi^2}{45}\frac{M_{\text{Pl}}M_{H_1}\sqrt{g_\rho(z)}}{1.66z^2}\sum_{i,j\in\text{SM},W_D,H_2}\langle\sigma v\rangle_{ij}\left(Y_i^{\text{eq}}Y_j^{\text{eq}} - Y_{N_m}^2\right)$$

$$-\frac{M_{\text{Pl}}z\sqrt{g_\rho(z)}}{1.66M_{H_1}^2 g_S(z)}\sum_{f_1,f_2\in\text{SM}}\langle\Gamma_{N_m\to S_m f_1 f_2}\rangle(Y_{N_m} - Y_{S_m}Y_{f_1}Y_{f_2})\theta\left(1 - \frac{M_{S_m} + M_{f_1} + M_{f_2}}{M_{N_m}}\right)$$

$$+\frac{2M_{\text{Pl}}z\sqrt{g_\rho(z)}}{1.66M_{H_1}^2 g_S(z)}\sum_{i=1,2}\langle\Gamma_{H_i\to N_m N_m}\rangle(Y_{H_i} - Y_{N_m}Y_{N_m})\theta\left(1 - \frac{2M_{N_m}}{M_{H_i}}\right)$$

$$\frac{dY_{S_m}}{dz} = \frac{4\pi^2}{45}\frac{M_{\text{Pl}}M_{H_1}\sqrt{g_\rho(z)}}{1.66z^2}\sum_{i,j\in\text{SM},W_D,H_2}\langle\sigma v\rangle_{ij}\left(Y_i^{\text{eq}}Y_j^{\text{eq}} - Y_{S_m}^2\right)$$

$$+\frac{M_{\text{Pl}}z\sqrt{g_\rho(z)}}{1.66M_{H_1}^2 g_S(z)}\sum_{f_1,f_2\in\text{SM}}\langle\Gamma_{N_m\to S_m f_1 f_2}\rangle(Y_{N_m} - Y_{S_m}Y_{f_1}Y_{f_2})\theta\left(1 - \frac{M_{S_m} + M_{f_1} + M_{f_2}}{M_{N_m}}\right)$$

$$+\frac{2M_{\text{Pl}}z\sqrt{g_\rho(z)}}{1.66M_{H_1}^2 g_S(z)}\sum_{i=1,2}\langle\Gamma_{H_i\to S_m S_m}\rangle(Y_{H_i} - Y_{S_m}Y_{S_m})\theta\left(1 - \frac{2M_{S_m}}{M_{H_i}}\right), \tag{4.11}$$

where $z \equiv M_{H_1}/T$, $\langle\sigma v\rangle_{AB\to CD}$ is the thermally-averaged cross section times velocity, $\langle\Gamma_{A\to BCD}\rangle$ is the thermally-averaged decay width, and $\theta(x)$ is the Heaviside step function. We present the relevant Feynman diagrams in appendix C.

In figure 8, the DM production by freeze-out and freeze-in mechanisms are shown. The green double-dot-dashed line corresponds to the WIMP DM production by the freeze-out
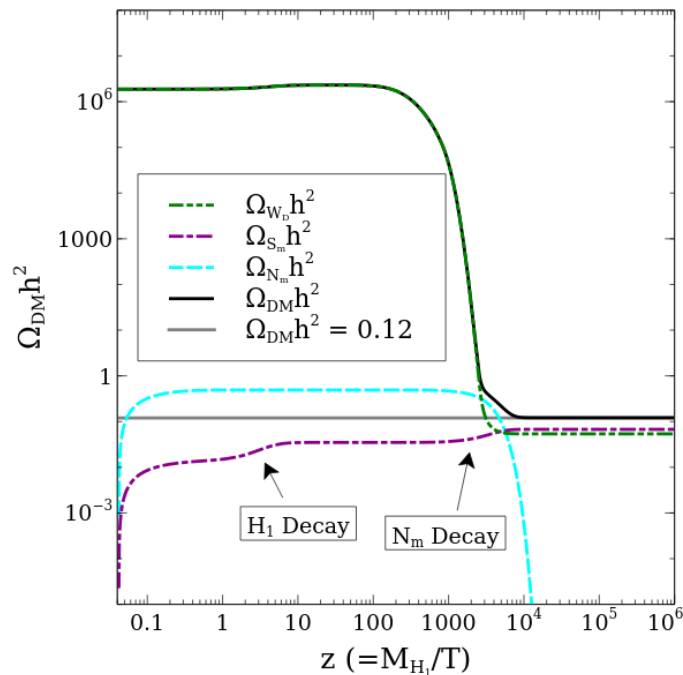
Figure 8. DM production by the freeze-out and freeze-in mechanisms and its evolution in terms of $z \equiv M_{H_1}/T$. The model parameters are chosen as $M_{N_m} = 300\,\text{GeV}$, $M_{S_m} = 20\,\text{GeV}$, $M_{W_D} = 1.04628\,\text{GeV}$, $\Lambda = 5.5 \times 10^{14}\,\text{GeV}$, $\kappa = \kappa' = \xi = \xi' = \alpha = \alpha' = 1$, $M_{H_2} = 2.212\,\text{GeV}$, $g_D = 3.1 \times 10^{-4}$, $\delta = 10^{-2}$, and $\sin\alpha = 8.17 \times 10^{-2}$. For the reheating temperature, we have used $T_R = 3\,\text{TeV}$. The green double-dot-dashed (purple dot-dashed) line corresponds to the WIMP (FIMP) DM relic density. The cyan dashed line represents the NLSP relic density. The sum of the WIMP and FIMP DM relic densities is depicted by the black solid line, while the grey solid line shows the present DM relic density measured by the Planck, $\Omega_{\text{DM}}h^2 = \Omega_{\text{Tot}}h^2 = 0.12$.

mechanism. It freezes out at $T \simeq M_{W_D}/20$ which corresponds to $z \simeq 2500$. The cyan dashed line represents the production of the NLSP N_m, which later decays to the FIMP DM S_m at $z \simeq 3500$. The NLSP is produced in the early Universe at $T \simeq 3000\,\text{GeV}$, i.e., $z \simeq 0.03$ through $2 \to 2$ processes present in our model. The purple dot-dashed line indicates the FIMP DM production via the freeze-in mechanism. At its initial production, we see a sharp rise at $z = 0.03$ which represents the production by the $2 \to 2$ processes like the NLSP case. There exists a second rise in the production shortly after $z = 1$ which is due to the decay of the SM-like Higgs, H_1. Finally, a third rise happens at $z \simeq 3500$ when the NLSP decays to the FIMP DM. The sum of the WIMP and FIMP DM relic densities is depicted by the black solid line, which coincides with the Planck measurement of total DM relic density $\Omega_{\text{Tot}}h^2 = 0.12$ today which is represented by the grey solid line. We have chosen the parameter values in such a way that the WIMP and FIMP DM contribute equally, namely $\Omega_{S_m}h^2 \approx \Omega_{W_D}h^2 \approx \Omega_{\text{Tot}}h^2/2$.

Dependence of the DM relic densities on the FIMP DM mass is shown in the LP of figure 9. One may see that the variation of the FIMP DM mass does not alter the WIMP DM relic density, which is depicted by double-dot-dashed lines. The dashed lines correspond
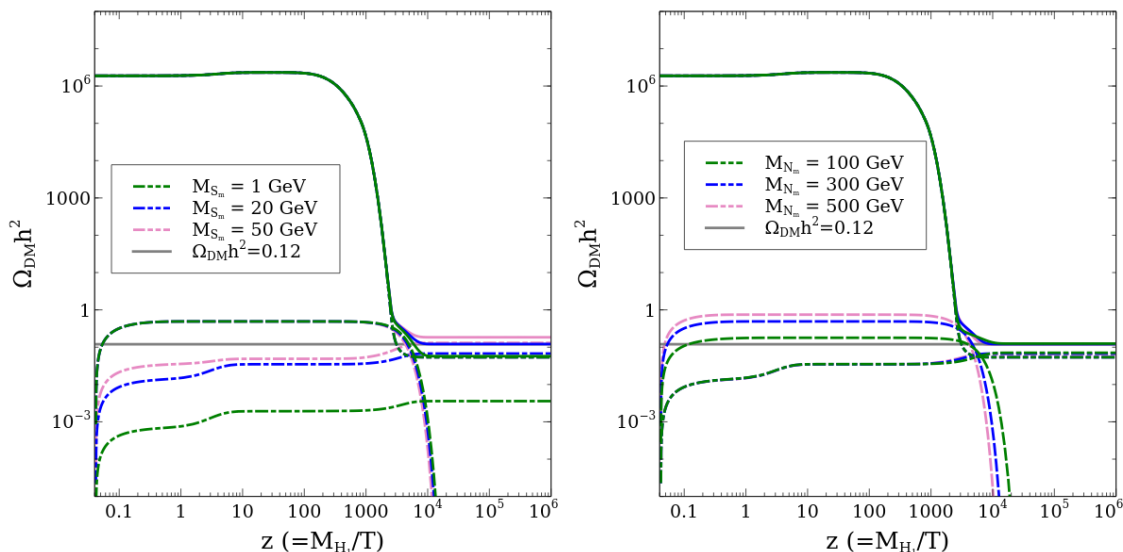
Figure 9. Dependence of the DM relic densities on three different values of the FIMP DM mass (left) and the NLSP mass (right). The other parameters are chosen as $M_{W_D} = 1.04628\,\text{GeV}$, $\Lambda = 5.5 \times 10^{14}\,\text{GeV}$, $\kappa = \kappa' = \xi = \xi' = \alpha = \alpha' = 1$, $M_{H_2} = 2.212\,\text{GeV}$, $g_D = 3.1 \times 10^{-4}$, $\delta = 10^{-2}$, and $\sin\alpha = 8.17 \times 10^{-2}$. For the reheating temperature, we have used $T_R = 3\,\text{TeV}$. For the left plot, $M_{N_m} = 300\,\text{GeV}$ is chosen, while $M_{S_m} = 20\,\text{GeV}$ is used for the right plot. The double-dot-dashed (dot-dashed) lines represent the WIMP (FIMP) DM relic densities, while the dashed lines indicate the NLSP relic densities. The solid lines are the sum of the FIMP and WIMP DM relic densities, while the grey solid line denotes the current DM relic density of 0.12.

to the NLSP (N_m) relic densities. The decay length of NLSP is not affected by the DM mass unless we choose $M_{N_m} \simeq M_{S_m} + M_{H_{1,2}}$. The dot-dashed lines below $\Omega_{\text{DM}}h^2 \simeq 10^{-1}$ are the FIMP DM evolutions. We see that, for $M_{S_m} = 1$ and $20\,\text{GeV}$, there is a slight rise in the DM density which corresponds to the FIMP DM production from the SM Higgs decay at around $z = 1$. This rise is, however, negligible for the $M_{S_m} = 50\,\text{GeV}$ case due to the phase space suppression from the SM Higgs decay. The second rise at $z \sim 3500$ happens when NLSP decays to the FIMP. Total DM relic density, which is the sum of the WIMP and FIMP relic densities, is represented by the solid lines. We see that the total DM relic density mainly follows the WIMP DM relic density. The RP of figure 9, shows the dependence of the DM relic densities on the NLSP mass. The NLSP masses are all above $100\,\text{GeV}$, so its production happens through $2 \to 2$ processes. The NLSP relic density varies linearly with its mass, and its contribution to the DM relic density is given by $(M_{N_m}/M_{S_m})\Omega_{N_m}h^2$. This is similar to the SuperWIMP mechanism [171] and associated with the conservation of the comoving number densities between two out-of-equilibrium species. For example, for a process $A \to B + \cdots$, if A and B are out of equilibrium, then one has $Y_A = Y_B$, and thus, $\Omega_A h^2/M_A = \Omega_B h^2/M_B$.

Figure 10 presents dependence of the DM relic densities on three different values Λ (LP) and g_D (RP). From the LP, one may see the significant changes in the FIMP DM and the NLSP relic densities with the variation of Λ. This behaviour is due to the fact that
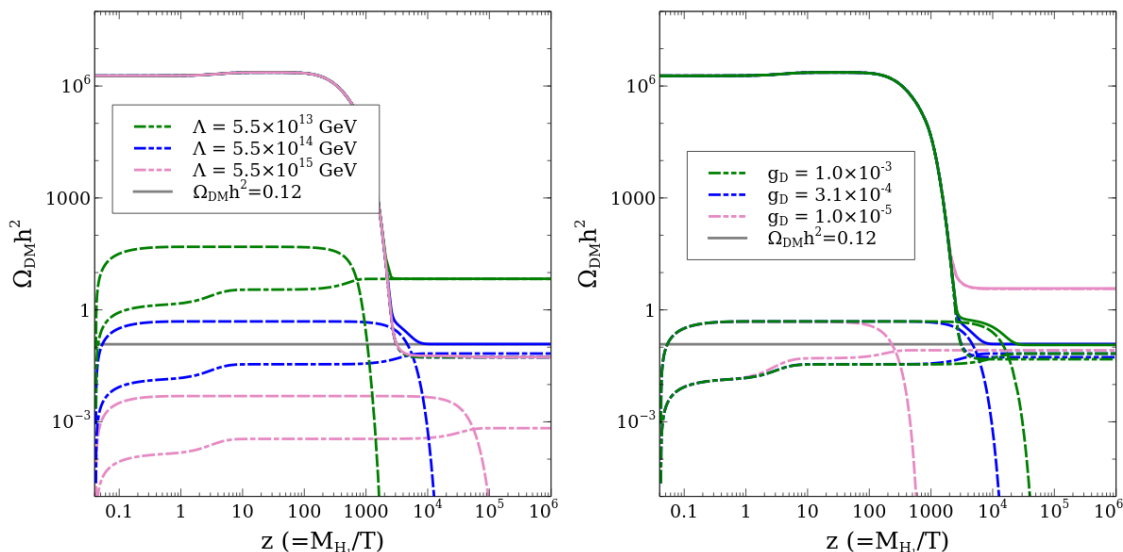
Figure 10. Dependence of the DM relic densities on three different values of Λ (left) and the dark gauge coupling g_D (right). The other parameters are kept the same as those given in figure 8. The double-dot-dashed (dot-dashed) lines represent the WIMP (FIMP) DM relic densities, while the dashed lines indicate the NLSP relic densities. The solid lines are the sum of the FIMP and WIMP DM relic densities, while the grey solid line denotes the current DM relic density of 0.12.

their production strength is inversely proportional to Λ. We see that the green lines, which correspond to $\Lambda = 5.5 \times 10^{13}$ GeV, have larger relic densities than the blue and pink lines, which respectively correspond to $\Lambda = 5.5 \times 10^{14}$ GeV and $\Lambda = 5.5 \times 10^{15}$ GeV. The RP of figure 10 shows the variation of the DM relic densities for three different values of the $U(1)_D$ gauge coupling g_D. The green lines are for $g_D = 10^{-3}$, the blue lines are for $g_D = 3.1 \times 10^{-4}$, and the pink lines are for $g_D = 10^{-5}$. We see that the $g_D = 10^{-5}$ case, which is depicted by the pink lines, has the largest WIMP DM relic density. It is because a smaller value of g_D reduces the WIMP DM annihilation cross-section ($W_D + W_D \to \mathrm{SM} + \mathrm{SM}$) which affects inversely the WIMP DM relic density. On the other hand, the FIMP DM relic density is controlled by the strength of the dark Higgs VEV $v_D = M_{W_D}/g_D$. The VEV v_D is linearly proportional to the coupling strength responsible for the FIMP DM production through the BSM Higgs decay. One interesting thing we may note is that g_D does not affect the NLSP production as its production is governed by the $2 \to 2$ processes. However, the NLSP decay depends on the VEV v_D; the NLSP decays faster with the increment of v_D or decrement of g_D. Moreover, FIMP DM production from the decays of the SM Higgs has an effect only when v_D is large enough; otherwise, the v_D-associated part in $H_1 \to S_m + S_m$ production is suppressed.

In figure 11, we show the dependence of the DM relic densities on three different values of M_{H_2} (LP) and M_{W_D} (RP). From the LP, we see that there is no effect of M_{H_2} on the FIMP DM production, while the effect on the WIMP DM production is significant. It is the case since the WIMP DM relic density is mainly controlled by how far we are from the resonance region of the second Higgs H_2. On the other hand, from the RP of figure 11, we
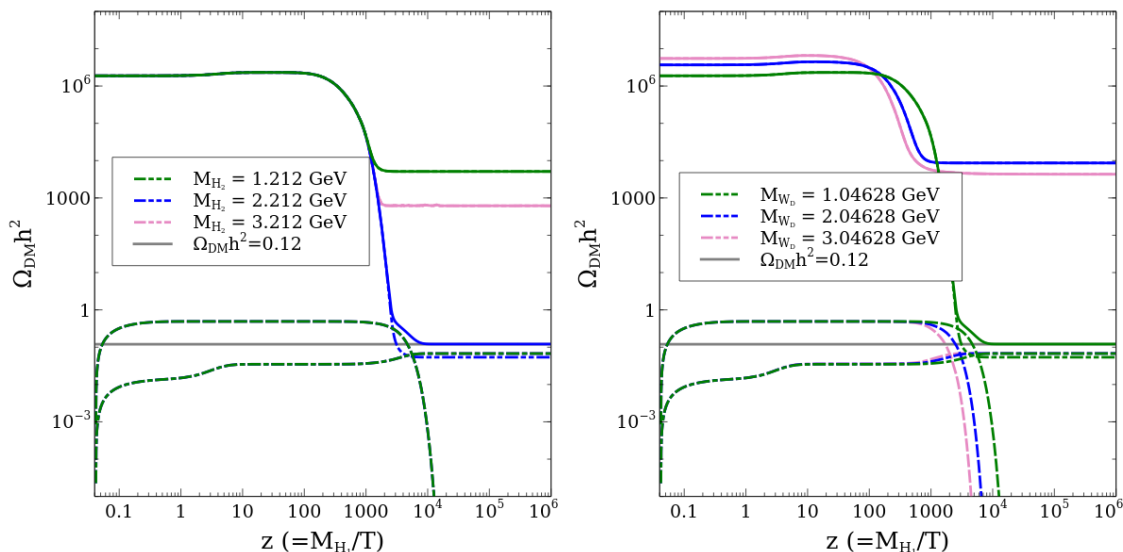
Figure 11. Dependence of the DM relic densities on three different values of the dark Higgs mass M_{H_2} (left) and the dark gauge boson WIMP mass M_{W_D} (right). The other parameters are kept the same as those given in figure 8. The double-dot-dashed (dot-dashed) lines represent the WIMP (FIMP) DM relic densities, while the dashed lines indicate the NLSP relic densities. The solid lines are the sum of the FIMP and WIMP DM relic densities, while the grey solid line denotes the current DM relic density of 0.12.

see that changing the WIMP DM mass affects both the WIMP and FIMP DM productions. The effect on the WIMP DM is due to the fact that, with the change of M_{W_D}, we are moving away from the resonance region of the second Higgs H_2, and thus we have more production of the WIMP DM. Additionally, the NLSP decay is proportional to the VEV $v_D = M_{W_D}/g_D$. Therefore, by increasing the value of M_{W_D}, the value of v_D increases as well, which triggers an early decay of NLSP.

4.2 Exploration of allowed parameter spaces

With the understandings we have acquired in section 4.1 by studying the behaviours of the DM relic densities near the point (3.3), we attempt to obtain allowed parameter regions amongst the different parameters after imposing that the DM relic density satisfies the range $0.01 \leq \Omega_{\mathrm{DM}} h^2 \leq 0.12$. The lower limit of 0.01 is to ensure more allowed points. Note, however, that our conclusion remains unchanged even if the 3σ range shown in eq. (4.1) is considered. We also discuss bounds on the WIMP DM parameters coming from the direct and indirect detections of DM. We perform parameter scans with the following parameter ranges:

$$1 \leq M_{S_m} \, [\mathrm{GeV}] \leq 100 \,, \quad 100 \leq M_{N_m} \, [\mathrm{GeV}] \leq 1000 \,, \quad 1 \leq M_{W_D} \, [\mathrm{GeV}] \leq 100 \,,$$

$$5.5 \times 10^{13} \leq \Lambda \, [\mathrm{GeV}] \leq 5.5 \times 10^{15} \,, \quad 10^{-4} \leq g_D \leq 10^{-1} \,, \quad 1.5 \leq \frac{M_{H_2}}{M_{W_D}} \leq 2.5 \,, \quad (4.12)$$

with the rest of the model parameters being fixed as those given in eq. (3.3). We have taken $T_R = 3 \, \mathrm{TeV}$ for the reheating temperature. The chosen range of the ratio M_{H_2}/M_{W_D} is due
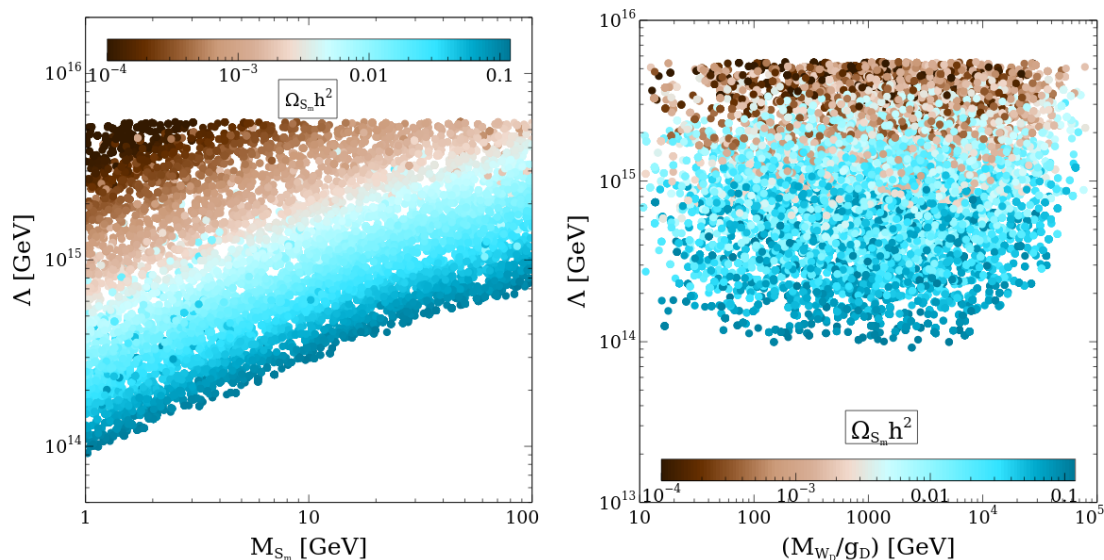
Figure 12. Allowed parameter space satisfying $0.01 \leq \Omega_{\rm DM}h^2 \leq 0.12$ in the M_{S_m} – Λ (left) and M_{W_D}/g_D – Λ (right) planes. The colour of the points represents the FIMP DM relic density.

to the observation that the WIMP DM mass needs to be close to the resonance region, as shown in figure 11.

The LP of figure 12 shows the allowed region in the M_{S_m} – Λ plane where the colour represents the FIMP DM relic density. One may easily see that, for a fixed value of the FIMP DM mass, increasing the value of Λ makes the FIMP contribution to DM relic density decrease, as the FIMP DM production is inversely proportional to Λ. The lower limit in the Λ value comes from the maximum allowed range for DM relic density, $\Omega_{\rm DM}h^2 = 0.12$, since the relic density is proportional to M_{S_m}/Λ^2. In the RP of figure 12, we present the allowed range in the M_{W_D}/g_D – Λ plane. One may again observe that, as we go to a higher value of Λ, we have a smaller FIMP DM contribution. The VEV $v_D = M_{W_D}/g_D$ linearly contributes to the FIMP DM relic density, and thus, for a higher value of v_D, we need a higher value of Λ to get the correct DM relic density value; we notice this in particular in the region $g_D < 10^{-3}$ and $10 < M_{W_D}\,[{\rm GeV}] < 100$. This correlation between v_D and Λ is observed for higher values of v_D, whereas we do not see such a correlation for lower values of v_D. In both the LP and RP of figure 12, we see that there is no upper bound on Λ. This is because such higher values of Λ reduce the FIMP DM relic density, and the DM relic density bound can be satisfied from the contribution of the WIMP DM.

The LP of figure 13 shows the allowed range in the M_{W_D} – M_{H_2}/M_{W_D} plane after imposing $0.01 \leq \Omega_{\rm DM}h^2 \leq 0.12$. It is clearly shown in the figure that, to obtain the WIMP DM relic density below 0.12, we need to stay near the resonance region, i.e., $M_{H_2} \sim 2M_{W_D}$. It is also clear that, when we are very close to the resonance region, we have a smaller WIMP contribution in the DM relic density, while a larger WIMP contribution is obtained as we depart from the resonance region. Moreover, we see that, for $M_{W_D} \simeq 62.5\,{\rm GeV}$, the dark Higgs mass M_{H_2} may take any value. This is due to the fact that the dominating contribution comes from the SM Higgs resonance. The RP of figure 13 shows the allowed
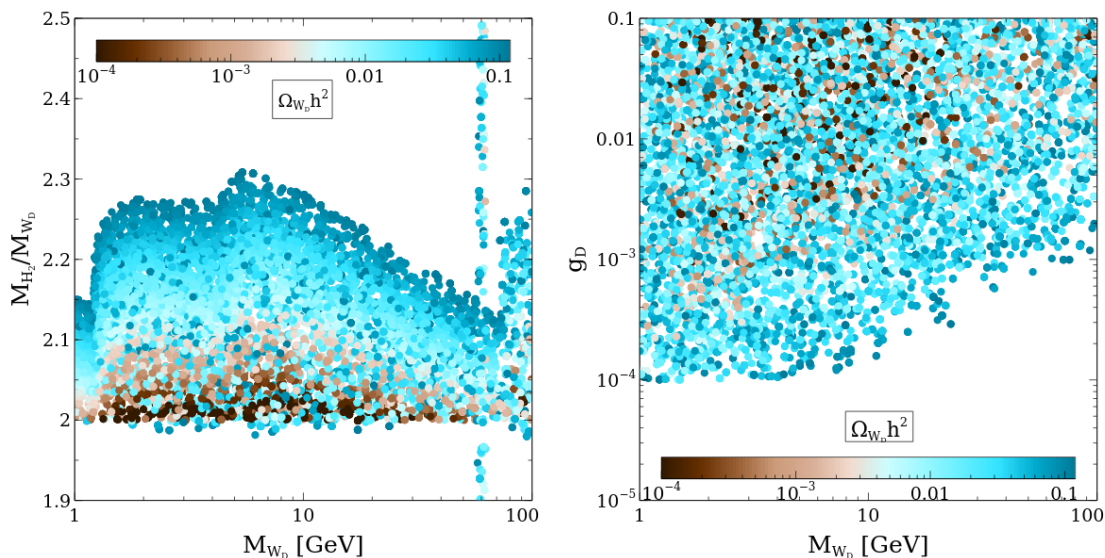
Figure 13. Allowed parameter space satisfying $0.01 \leq \Omega_{\text{DM}} h^2 \leq 0.12$ in the $M_{W_D} - M_{H_2}/M_{W_D}$ (left) and $M_{W_D} - g_D$ (right) planes. The colour of the points represents the WIMP DM relic density.

region in the $M_{W_D} - g_D$ plane after imposing $0.01 \leq \Omega_{\text{DM}} h^2 \leq 0.12$. One may see from the figure that, if we increase the value of g_D, one may have a smaller contribution of WIMP DM. This happens because the annihilation cross section increases with g_D, and the WIMP DM relic density is inversely proportional to annihilation cross section. For higher values of $M_{W_D} \gtrsim 10$ GeV, we see no allowed point in the range $10^{-4} \lesssim g_D \lesssim 10^{-3}$ as the region has a dominating FIMP DM contribution due to the high value of the VEV v_D.

How close one needs to be to the resonance region is studied in figure 14 where the WIMP DM relic density is shown in terms of the mixing angle $\sin\theta$ and $r \equiv 2M_{W_D}/M_{H_2}$. The parameter r quantifies the closeness to the resonance region, and $r = 1$ corresponds to the exact resonance point. We find that r typically takes a value between 0.92 and 0.98, depending on the value of the mixing angle, if we ask for the WIMP DM component to be a significant part of the total relic density. We observe that the window for a WIMP DM relic density of at least 10% of the total DM relic density is narrower for smaller values of the mixing angle. At a fixed value of r, the relic density decreases as the value of $\sin\theta$ increases. One may understand this as follows: The process keeping the WIMP DM in thermal equilibrium is $\text{DM} + \text{DM} \leftrightarrow \text{SM} + \text{SM}$, and it is mediated by H_2. We thus find that the cross section is proportional to $\cos^2\theta \sin^2\theta$. Higher values of r mean being closer to the resonant point where the cross section increases. Therefore, the relic density decreases following the standard behaviour, $\Omega_{\text{WIMP}} h^2 \sim 1/\langle\sigma v\rangle$. Once we depart too much from the resonance region, we may overproduce the WIMP DM and overclose the Universe.

Figure 15 shows the allowed region in the $M_{W_D} - (\Omega_{W_D}/\Omega_{\text{Tot}})\sigma_{\text{SI}}$ (LP) and $M_{W_D} - (\Omega_{W_D}/\Omega_{\text{Tot}})\langle\sigma v\rangle_{b\bar{b}}$ (RP) planes, together with various direct and indirect detection bounds that are depicted by solid lines. Note that we have rescaled the y-axes by the amount of the WIMP DM relic density compared to the total DM in the Universe $\Omega_{\text{Tot}} h^2 = 0.12$. The LP of figure 15 may be easily understood with the direct detection expression given by
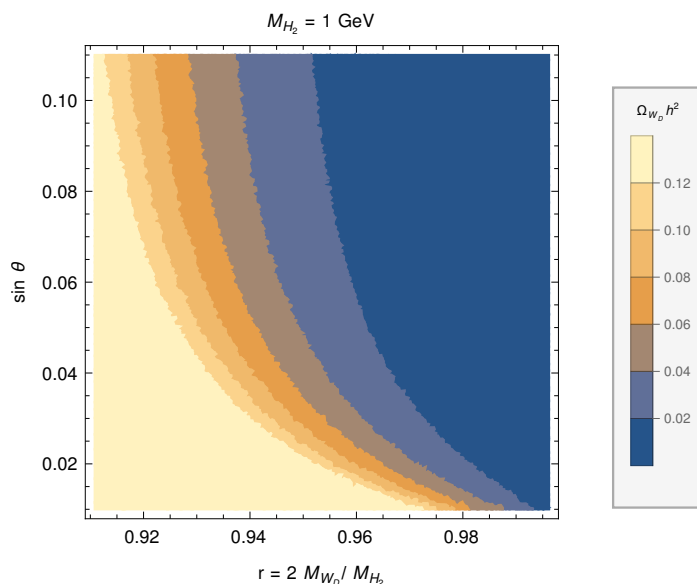
Figure 14. WIMP DM relic density as a function of the mixing angle $\sin\theta$ and $r \equiv 2M_{W_D}/M_{H_2}$ that quantifies the closeness to the resonance region. The exact resonance point is where $r = 1$. For this example, we have set $M_{H_2} = 1\,\mathrm{GeV}$. The other relevant parameter is g_D, and it is fixed as $g_D = 10^{-4}$. In order to have a significant amount of WIMP relic density while not overproducing, we need to be near the range of $0.92 \lesssim r \lesssim 0.98$ for $\sin\theta < 0.1$.
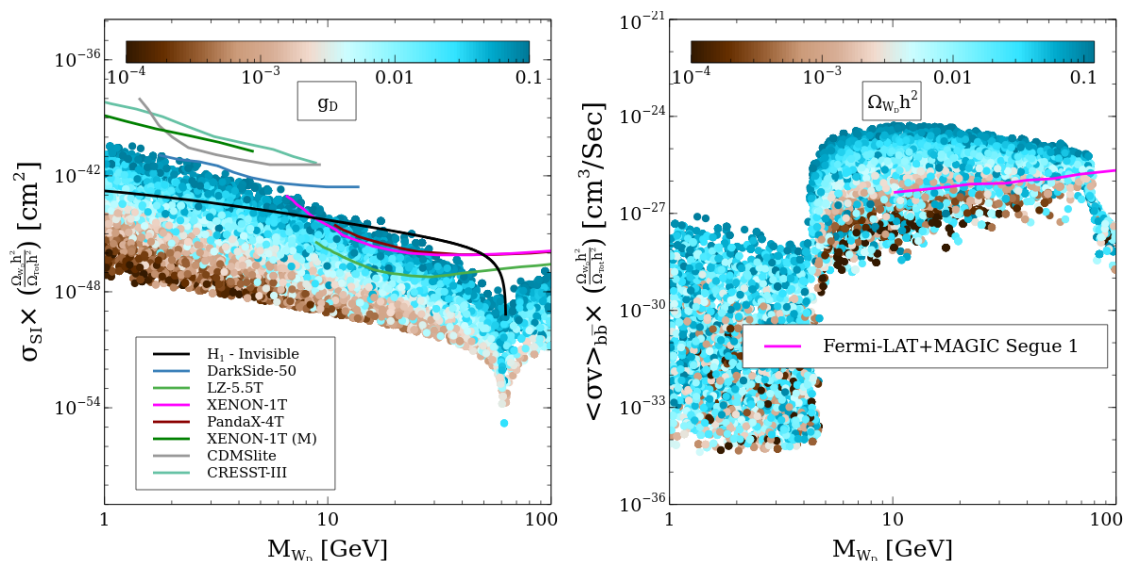

Figure 15. Allowed parameter space satisfying $0.01 \leq \Omega_{\mathrm{DM}}h^2 \leq 0.12$ in the $M_{W_D} - (\Omega_{W_D}/\Omega_{\mathrm{Tot}})\sigma_{\mathrm{SI}}$ (left) and $M_{W_D} - (\Omega_{W_D}/\Omega_{\mathrm{Tot}})\langle\sigma v\rangle_{b\bar{b}}$ (right) planes. Here, $\Omega_{\mathrm{Tot}}h^2 = 0.12$ is total DM relic density today. The black solid line in the left panel indicates the Higgs invisible decay constraint. Various direct and indirect detection bounds are also overlaid with coloured solid lines; see text for detailed explanation. The colour of the points represents the value of the dark gauge coupling g_D (left) and the WIMP DM relic density (right).

eq. (4.2), which states that $\sigma_{\rm SI}$ is proportional to g_D^2. One may estimate the percentage of the WIMP DM relic that each sample point corresponds to with the help of the RP of figure 13. Comparing the LP of figure 15 and RP of figure 13, one can easily see that lower values of g_D correspond to lower values of $\sigma_{SI}(\propto g_D^2)$ and higher values of the WIMP DM relic density as the density is inversely proportional to g_D^2. A sharp dip at $M_{W_D} \simeq 62.5\,{\rm GeV}$ happens because of the mutual cancellation between the SM Higgs- and the BSM Higgs-mediated processes as one may see from eq. (4.2). A part of the $M_{W_D} > 7\,{\rm GeV}$ region is already ruled out by the different direct detection experiments such as XENON-1T [19], PandaX-4T [159, 160], and LUX-ZEPLIN-5.5T [158]. The region of DM mass below $7\,{\rm GeV}$ will be explored by DarkSide-50 [161, 162], XENON-1T(M) [163], CDMSlite [164], and CRESST-III [165, 166]. The black solid line corresponds to the bound from the Higgs invisible decay which is obtained by staying near the dark Higgs resonance region, i.e., $M_{H_2} \sim 2M_{W_D}$, so that the WIMP DM never becomes over-abundant. The region above the black solid line is already ruled out by the current bound on the branching of the Higgs invisible decay mode. We note that our model predicts much lower values for $\sigma_{\rm SI}$ compared to the aforementioned bounds. From the RP of figure 15, we see that there is a dip in $\langle \sigma v \rangle_{b\bar{b}}$ for the WIMP DM mass below $5\,{\rm GeV}$. This is due to the fact that, for this range, the channel $W_D W_D \to b\bar{b}$ is not active. The region of $M_{W_D} \gtrsim 10\,{\rm GeV}$ is constrained by the Fermi-LAT + MAGIC Segue 1 data [21]. We observe that most of the parameter space which contributes dominantly to the DM relic is already ruled out by the indirect detection bound. We have also checked the present bounds on the DM annihilation to $\mu^+\mu^-$ and $\tau^+\tau^-$, and we present the results in appendix D.

5 First-order phase transitions and associated gravitational waves

The extra dark U(1)$_D$ Higgs field not only gives a mass to the WIMP DM W_D, but it also changes the vacuum evolution. We study the evolution of the vacuum state and the dynamics of the phase transition in this section. We first compute the one-loop finite-temperature effective potential,

$$V_{\rm eff} = V^{(0)} + V_{\rm CW}^{(1)} + V_T^{(1)}\,, \tag{5.1}$$

where $V^{(0)}$ is the tree-level scalar potential, $V_{\rm CW}^{(1)}$ is the one-loop Coleman-Weinberg potential, and $V_T^{(1)}$ is the finite-temperature correction. In terms of the background fields $\bar{H}$ and $\bar{H}_D$ of the SM Higgs and the U(1)$_D$ dark Higgs, the tree-level scalar potential is given by

$$V^{(0)} = \frac{1}{2}\mu_h^2 \bar{H}^2 + \frac{1}{2}\mu_D^2 \bar{H}_D^2 + \frac{1}{4}\lambda_h^2 \bar{H}^4 + \frac{1}{4}\lambda_D^2 \bar{H}_D^4 + \frac{1}{4}\lambda_{hD}^2 \bar{H}^2 \bar{H}_D^2\,. \tag{5.2}$$

The Coleman-Weinberg potential can generically be written as

$$V_{\rm CW}^{(1)} = \pm \sum_i n_i \frac{M_i^4(\bar{H}, \bar{H}_D)}{64\pi^2} \left[\ln \frac{M_i^2(\bar{H}, \bar{H}_D)}{\bar{\mu}^2} - c_i \right]\,, \tag{5.3}$$

where the $+$ $(-)$ sign is for bosons (fermions), n_i is the number of degrees of freedom of the species i, M_i is the field-dependent mass, the constants c_i are $1/2$ for transverse

gauge bosons and 2/3 for the rest, and $\bar{\mu}$ is the renormalisation scale. The expressions for the field-dependent masses M_i and n_i are summarised in appendix E. Depending on the choice of the renormalisation scale $\bar{\mu}$, the effective potential V_{eff} changes, and hence one may arrive at different results. This renormalisation scale dependence has been explored in e.g. refs. [172, 173].[4] Together with the gauge dependence issue, we do not attempt to address the issue of the renormalisation scale dependence as it goes beyond the scope of the current work. We thus ignore the one-loop Coleman-Weinberg corrections in the followings by assuming that the renormalisation scale $\bar{\mu}$ is chosen in such a way that the Coleman-Weinberg corrections are minimised. The finite-temperature correction is given by [179]

$$V_T^{(1)} = \frac{T^4}{2\pi^2} \sum_i n_i I_{\pm} \left(\frac{M_i^2(\bar{H}, \bar{H}_D)}{T^2} \right) , \tag{5.4}$$

with

$$I_{\pm}(x^2) = \pm \int_0^{\infty} dy\, y^2 \ln \left(1 \mp e^{-\sqrt{y^2+x^2}} \right) , \tag{5.5}$$

where I_+ is for bosons and I_- is for fermions. The re-summed ring diagrams are taken into account by replacing the field-dependent masses as [180]

$$M_i^2 \to \widetilde{M}_i^2 = M_i^2 + \Pi_i(T) , \tag{5.6}$$

where $\Pi_i(T)$ are the thermal masses [181]. We present the thermal mass expressions in appendix F. Up to the leading $\mathcal{O}(T)$ order, the effective potential is thus given by

$$\begin{aligned}
V_{\text{eff}} = &\frac{1}{2} \left(\mu_h^2 + \Pi_H \right) \bar{H}^2 + \frac{1}{2} \left(\mu_D^2 + \Pi_{H_D} \right) \bar{H}_D^2 \\
&+ \frac{1}{4} \lambda_h^2 \bar{H}^4 + \frac{1}{4} \lambda_D^2 \bar{H}_D^4 + \frac{1}{4} \lambda_{hD}^2 \bar{H}^2 \bar{H}_D^2 - E^{\text{SM}} \bar{H}^3 T + \cdots ,
\end{aligned} \tag{5.7}$$

where $E^{\text{SM}} \equiv (2g_2^3 + \sqrt{g_1^2 + g_2^2}^3)/(32\pi)$ and '$\cdots$' include sub-leading, negligible terms. Note that we have assumed that the dark gauge coupling g_D is small enough not to affect the leading-order terms.

In the presence of the extra Higgs field, FOPTs may arise. FOPTs with a dark U(1)$_D$ have been studied in e.g. refs. [112, 182–184]. For studies of the phase transition with an extra scalar field, see, e.g., refs. [153, 172, 178, 185–189]. In particular, in ref. [153] where the studied scalar potential has the same form as eq. (5.7), it was shown both analytically and numerically that the FOPTs could be strong, characterised by $v_c/T_c \gtrsim 1$. Here, T_c is the critical temperature at which the potential minima become degenerate, and v_c is the VEV of the SM Higgs field at T_c. It indicates that one of the Sakharov conditions for successful electroweak baryogenesis can be fulfilled [190]. Since the scalar field space is now two-dimensional due to the extra Higgs field, one may achieve either one-step or two-step phase transitions. Noting that the VEV of the U(1)$_D$ Higgs is non-zero at zero

---

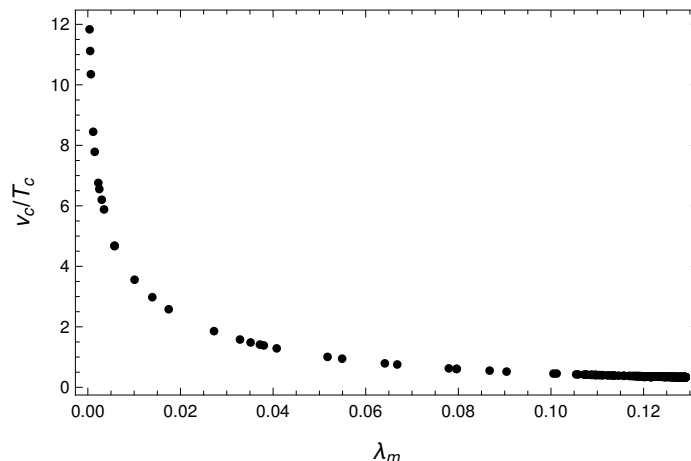[4]See also e.g. refs. [172–178] for the gauge dependence issue.

Figure 16. Numerically computed v_c/T_c values as a function of $\lambda_m \equiv \lambda_h - \lambda_{hD}^2/(4\lambda_D)$. Being in agreement with the analytical expression (5.8), strong FOPTs, $v_c/T_c \gtrsim 1$, are achieved for small values of λ_m, or equivalently, small values of the dark $\mathrm{U}(1)_D$ Higgs mass. We note that our result matches with the one presented in ref. [153].

temperature, the one-step phase transition has the pattern $(\langle H \rangle, \langle H_D \rangle) = (0, 0) \to (v, v_D)$, while the two-step phase transition may occur via $(\langle H \rangle, \langle H_D \rangle) = (0, 0) \to (0, v_D') \to (v, v_D)$ or $(\langle H \rangle, \langle H_D \rangle) = (0, 0) \to (v', 0) \to (v, v_D)$. For the two-step phase transition of the pattern $(\langle H \rangle, \langle H_D \rangle) = (0, 0) \to (0, v_D') \to (v, v_D)$, the second step breaks the electroweak symmetry, giving [153]

$$\frac{v_c}{T_c} = \frac{2E^{\mathrm{SM}}}{\lambda_h - \lambda_{hD}^2/(4\lambda_D)} = \frac{4E^{\mathrm{SM}}v^2}{M_{H_1}^2}\left(1 + \sin^2\theta \, \frac{M_{H_1}^2 - M_{H_2}^2}{M_{H_2}^2}\right). \tag{5.8}$$

One may see that strongly FOPTs, $v_c/T_c \gtrsim 1$, can be achieved when the dark Higgs is lighter than the SM Higgs. The one-step phase transition shows a similar behaviour [153]. Utilising the publicly available tool `CosmoTransitions` [191], we numerically compute v_c/T_c for a wide range of the parameter space and present the result in figure 16. The explored parameter range is as follows:

$$0.01 \leq M_{H_2}\,[\mathrm{GeV}] \leq 100, \quad -0.1 \leq \sin\theta \leq 0.1,$$
$$10 \leq v_D\,[\mathrm{GeV}] \leq 10^4, \qquad 10^{-5} \leq g_D \leq 10^{-2}. \tag{5.9}$$

We note that these four input parameters are the only relevant model parameters. The other model parameters can be derived from the above input parameters. The x-axis of figure 16 is defined as $\lambda_m \equiv \lambda_h - \lambda_{hD}^2/(4\lambda_D)$. We observe that strong FOPTs could be achieved for small values of λ_m, which is in good agreement with both the analytical estimate (5.8) and the results of ref. [153].

FOPTs may produce observable stochastic GWs [95]. There are three main contributions to the GWs from the FOPT: bubble wall collisions $\Omega_{\mathrm{col}}h^2$, sound wave in plasma $\Omega_{\mathrm{sw}}h^2$, and the magneto-hybrodynamic turbulence $\Omega_{\mathrm{turb}}h^2$. The total GWs are then $\Omega_{\mathrm{GW}}h^2 \simeq \Omega_{\mathrm{col}}h^2 + \Omega_{\mathrm{sw}}h^2 + \Omega_{\mathrm{turb}}h^2$. The GWs coming from the bubble wall collisions are given

by [108]

$$\Omega_{\text{col}}h^2 = 1.67 \times 10^{-5} \left(\frac{\mathcal{H}_*}{\beta}\right)^2 \left(\frac{\kappa_\phi \alpha}{1+\alpha}\right)^2 \left(\frac{100}{g_*}\right)^{\frac{1}{3}} \left(\frac{0.11 v_w^3}{0.42 + v_w^2}\right) \left(\frac{3.8\,(f/f_{\text{col}})^{2.8}}{1 + 2.8\,(f/f_{\text{col}})^{3.8}}\right),$$
(5.10)

while the turbulence contribution is [108]

$$\Omega_{\text{turb}}h^2 = 3.35 \times 10^{-4} \left(\frac{\mathcal{H}_*}{\beta}\right) \left(\frac{\kappa_{\text{turb}} \alpha}{1+\alpha}\right)^{\frac{3}{2}} \left(\frac{100}{g_*}\right)^{\frac{1}{3}} \left(\frac{v_w\,(f/f_{\text{turb}})^3}{[1 + (f/f_{\text{turb}})]^{\frac{11}{3}}\,(1 + 8\pi f/h_*)}\right),$$
(5.11)

where

$$h_* = 1.65 \times 10^{-5}\,\text{Hz} \left(\frac{T_*}{100\text{GeV}}\right) \left(\frac{g_*}{100}\right)^{\frac{1}{6}}.$$
(5.12)

Finally, the sound-wave contribution to the GW signal can be expressed as [188, 192–194]

$$\Omega_{\text{sw}}h^2 = 4.80 \times 10^{-6} \min\left\{1, \frac{2(8\pi)^{1/3}}{\sqrt{3}} v_w \left(\frac{\mathcal{H}_*}{\beta}\right) \sqrt{\frac{1+\alpha}{\kappa_v \alpha}}\right\}$$
$$\times \left(\frac{\mathcal{H}_*}{\beta}\right) \left(\frac{\kappa_v \alpha}{1+\alpha}\right)^2 \left(\frac{100}{g_*}\right)^{\frac{1}{3}} v_w\,(f/f_{\text{sw}})^3 \left(\frac{7}{4 + 3\,(f/f_{\text{sw}})^2}\right)^{\frac{7}{2}}.$$
(5.13)

For the expressions for f_{col}, f_{sw}, f_{turb}, v_w, κ, κ_v, and κ_{trub}, see appendix G.

Three parameters that play the key roles in the GW signal are

$$\alpha = \frac{\rho_{\text{vac}}}{\rho_{\text{rad}}^*}, \qquad \frac{\beta}{\mathcal{H}_*} = T_* \frac{dS_{\text{E}}}{dT}\bigg|_{T_*}, \quad \text{and} \quad T_*,$$
(5.14)

where $S_{\text{E}} = S_3/T$ is the Euclidean action of a bubble with S_3 being the three-dimensional action, ρ_{vac} the released energy density during the phase transition, and $\rho_{\text{rad}}^* = g_* \pi^2 T_*^4/30$, with g_* being the number of effective degrees of freedom at $T = T_*$. We take T_* to be the nucleation temperature T_n. We employ CosmoTransitions [191] to numerically compute the three key parameters, α, $\beta/\mathcal{H}_*$, and the nucleation temperature T_n. In figure 17, we present the FOPT-associated GW signals for three BPs together with the sensitivity curves of future space-based GW experiments such as LISA, DECIGO, and BBO. The three BPs, that account for not only the neutrino masses and the correct DM relic density, but also the strong FOPTs, are summarised in table 2. One may notice that the three BPs have different DM compositions. In the case of the first BP (BP1), both the WIMP and FIMP contribute equally to the total DM relic density, while the BP2 (BP3) is mostly composed of the FIMP (WIMP) DM. We see from figure 17 that the GW signals for all the BPs are well within the reach of the detectability threshold of BBO, DECIGO, and Ultimate-DECIGO.
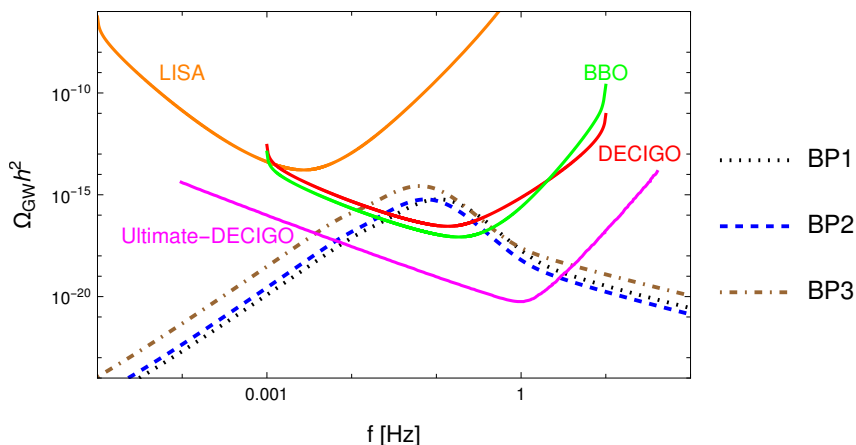
Figure 17. FOPT-associated GW spectra for our three BPs summarised in table 2. The black dotted line corresponds to the first BP, the blue dashed line depicts the second BPs, and the brown dot-dashed line represents the third BP. The sensitivity curves of future space-base GW experiments, including LISA, BBO, DECIGO, and Ultimate-DECIGO, are shown as well. We consulted ref. [195] for the data for LISA, BBO, and DECIGO, and ref. [196] for the Ultimate-DECIGO.

BPs	v_D [TeV]	M_{H_2} [GeV]	$\sin\theta$	g_D [10^{-4}]	α	$\frac{\beta}{\mathcal{H}_*}$	T_n [GeV]	$\frac{v_c}{T_c}$	$\frac{\Omega_{\mathrm{WIMP}}}{\Omega_{\mathrm{Tot}}}$	$\frac{\Omega_{\mathrm{FIMP}}}{\Omega_{\mathrm{Tot}}}$
BP1	3.37	2.21	0.082	3.1	0.238	13671	34.43	4.67	0.46	0.54
BP2	0.673	2.77	-0.076	19.7	0.139	6760.0	46.67	3.56	0.044	0.956
BP3	4.63	1.0	0.060	1.0	0.461	13820	21.58	6.76	0.87	0.13

Table 2. Three BPs. The first four columns represent the input model parameters, the fifth, sixth, and the seventh columns are GW-related quantities, the eighth column shows the strength of the FOPT. The last two columns denote the WIMP and FIMP contributions to the total DM relic density $\Omega_{\mathrm{Tot}}h^2 = 0.12$; for the first BP, both the WIMP and FIMP equally contribute to the total DM relic density, while the second (third) BP is mostly composed of FIMP (WIMP) DM. In all the three cases, the LFV bounds are satisfied, and the neutrino masses can successfully be generated. The GW signals corresponding to the three BPs are shown in figure 17.

6 Collider searches

The present work deals with the WIMP and FIMP-type DMs. Due to the feeble interaction of the FIMP, it is difficult to probe it at collider experiments. We can, however, focus on general search strategies for BSM particles in the context of the present work. In particular, we may study the production of the second Higgs H_2 at the pp or e^+e^- colliders and look for its subsequent decay. Suitably adjusting the WIMP DM mass allows the second Higgs to decay mainly to the WIMP DM, and we may look for the missing energy with mono-jet or di-jet signals in the final state. Otherwise, if H_2 does not dominantly decay to the WIMP DM, then it will decay to the SM particles such as the SM Higgs. See, e.g., refs. [45, 197].

The relevant signal channels for our current study at the pp collider would be

$$pp \rightarrow pj + H_2 \rightarrow pj + \slashed{E}_T \ (p \geq 1),$$
$$\rightarrow nj + ml \ (n, m \geq 1), \tag{6.1}$$

where j corresponds to the initial or final state jets, l is associated with the SM lepton, and $\slashed{E}_T$ is the transverse missing energy. Similar to the SM Higgs searches, we can also investigate

$$e^+ e^- \rightarrow Z H_2 \rightarrow nj + pl \ (n, p \rightarrow 1)$$
$$\rightarrow nj + pl + \slashed{E}_T, \tag{6.2}$$

at the $e^+ e^-$ collider. The exact values of the integers, n, m, and p, depend on the production cross section and dominance of the associated backgrounds. Moreover, exploring the singlet fermions (S_L, N_L) of our model at different colliders is an interesting direction; see, e.g., ref. [197]. Further comments require a full-fledged collider study which is out of the scope of the current work, and we leave it for future study.

7 Conclusion

We have studied an extension of the Standard Model that accounts for the dark matter and the smallness of the neutrino masses under the extended seesaw framework. In our model, two sets of three-generation neutrinos are introduced; the first two generations provide the light neutrinos with a mass, and the third-generation neutrinos become FIMP-like particles. Amongst these FIMP-like particles, the heavier one eventually decays into the lighter one, and thus, we have the lighter third-generation neutrino as the FIMP dark matter candidate. Our model also contains a WIMP dark matter candidate, namely the dark $U(1)_D$ gauge boson. Thus, a two-component WIMP-FIMP dark matter scenario naturally arises in our model.

We have explored allowed parameter spaces by using the lepton flavour violating bounds as well as the neutrino oscillation data. Much of the parameter spaces are already tightly constrained, but we have shown that there are viable parameter regions which are free from the constraints. Prospects of various future experiments have been discussed as well. Interestingly, the contribution to the FIMP dark matter relic density coming from neutrinos scattering is found to be up to a 3% of the total relic density for the range of the model parameters considered in our study. We have also discussed the dependence of the relic density on the model parameters. Utilising publicly available tools, we have performed extensive numerical parameter scans in order to study the evolutions of the dark matter candidates. Parameter spaces compatible with the bounds from (in-)direct detection and collider searches are presented. In particular, we have showed regions where a two-component dark matter scenario is realised and testable by future (in-)direct experiments.

The dark $U(1)_D$ Higgs field plays a major role in the FIMP and WIMP dark matter productions. In addition, the extra scalar field also changes the evolution of the vacuum state in the scalar sector, making a first-order phase transition possible. We have demonstrated

that the strength of the electroweak first-order phase transition, quantified by the quantity v_c/T_c, where T_c is the critical temperature and v_c is the SM Higgs vacuum expectation value at T_c, may become larger than unity for small values of the dark $U(1)_D$ Higgs mass. Therefore, one of the essential ingredients for a successful electroweak baryogenesis is achieved in our model. We have also studied stochastic gravitational waves associated with the first-order phase transitions and showed that the gravitational wave signals are strong enough to be detectable by future experiments such as BBO and DECIGO.

Three benchmark points, that explicitly demonstrate the capability of *i)* having a correct dark matter relic density, *ii)* generating the non-zero neutrino masses with the extended seesaw mechanism, *iii)* achieving a strongly first-order phase transition, and *iv)* emitting stochastic gravitational waves detectable by future experiments, are presented. Thus, the model studied in this work has an exciting potential detectability not only with future (in-)direct detection experiments and collider searches, but also with future gravitational wave experiments.

Acknowledgments

A WIMP DM decay width through kinetic mixing

In the presence of the mixing between the WIMP DM and the $U(1)_Y$ gauge boson, the DM may decay to, e.g., electrons, through the coupling between the DM and SM fermions [123]. For simplicity, we consider the decay of the DM to electrons. The decay width is then given by

$$\Gamma_{W_D \to ee} = \frac{M_{W_D} g_{W_D ee}^2}{12\pi} \left(1 + \frac{2m_e^2}{M_{W_D}^2} \right) \sqrt{1 - \frac{4m_e^2}{M_{W_D}^2}}, \tag{A.1}$$

where $g_{W_D ee} = 3e\zeta/(4\cos\theta_w)$, $e = \sqrt{4\pi\alpha}$, α is the fine-structure constant, θ_w is the weak angle, and ζ is the gauge kinetic mixing parameter introduced in (2.1). Considering the DM mass of $10\,\text{GeV}$, and requiring the lifetime of the DM to be is larger than the age of the universe, we get an upper bound on the gauge kinetic mixing parameter as $\zeta < 10^{-20}$. When the decay of the DM to the SM fermions is open, the γ-ray observation may become relevant [125]. In this case, the DM lifetime should be greater than 10^{29}s [125], which puts an even stronger bound of $\zeta < 10^{-26}$.
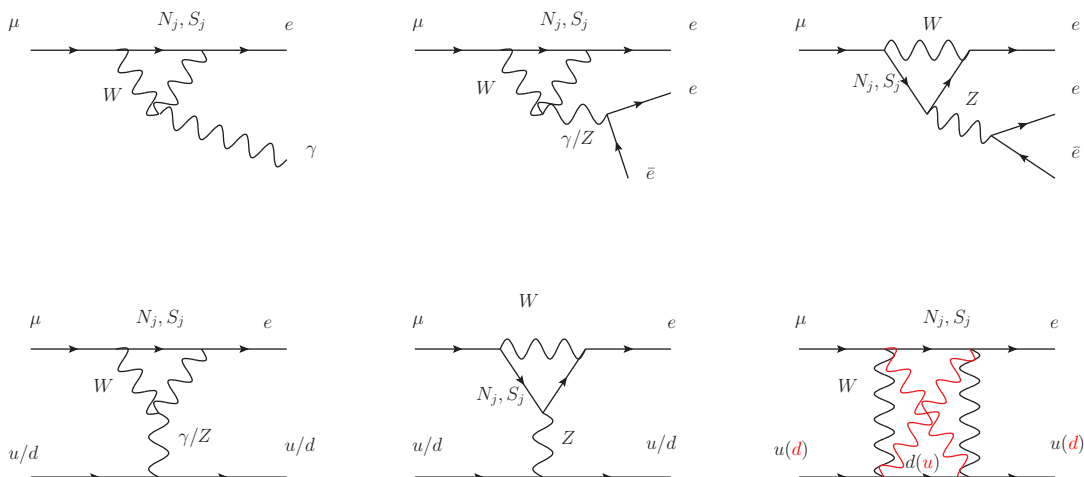
Figure 18. Feynman diagrams for LFV processes.

B Quartic couplings

The scalar quartic couplings may be written in terms of the mixing angle and masses of the physical Higgses as follows:

$$
\begin{aligned}
\lambda_h &= \frac{M_{H_1}^2 \cos^2\theta + M_{H_2}^2 \sin^2\theta}{2v^2}\,, \\
\lambda_D &= \frac{M_{H_1}^2 \sin^2\theta + M_{H_2}^2 \cos^2\theta}{2v_D^2}\,, \\
\lambda_{hD} &= \frac{(M_{H_1}^2 - M_{H_2}^2)\sin 2\theta}{2vv_D}\,.
\end{aligned} \tag{B.1}
$$

C Feynman diagrams

Figure 18 shows the diagrams which contribute to the processes $\mu \to e\gamma$, $\mu \to ee\bar{e}$, and μ-to-e conversion. We have considered these diagrams for the discussion of the LFV bounds. The Feynman diagrams relevant for our DM analysis are shown in figure 19.

D DM annihilation to $\tau^+\tau^-$ and $\mu^+\mu^-$

The LP and RP of figure 20 present the DM annihilation to $\tau^+\tau^-$ and $\mu^+\mu^-$, respectively, together with the bounds from FERMI-LAT [167, 168], CMB [168], and AMS [168, 169] data. We find that our model predicts $\langle\sigma v\rangle$ orders of magnitude lower than the current bound. We expect that our model parameter space may be explored in future by different ongoing indirect detection experiments. Finally, we note that the DM annihilation to e^+e^- is many orders below than the current bound as well.
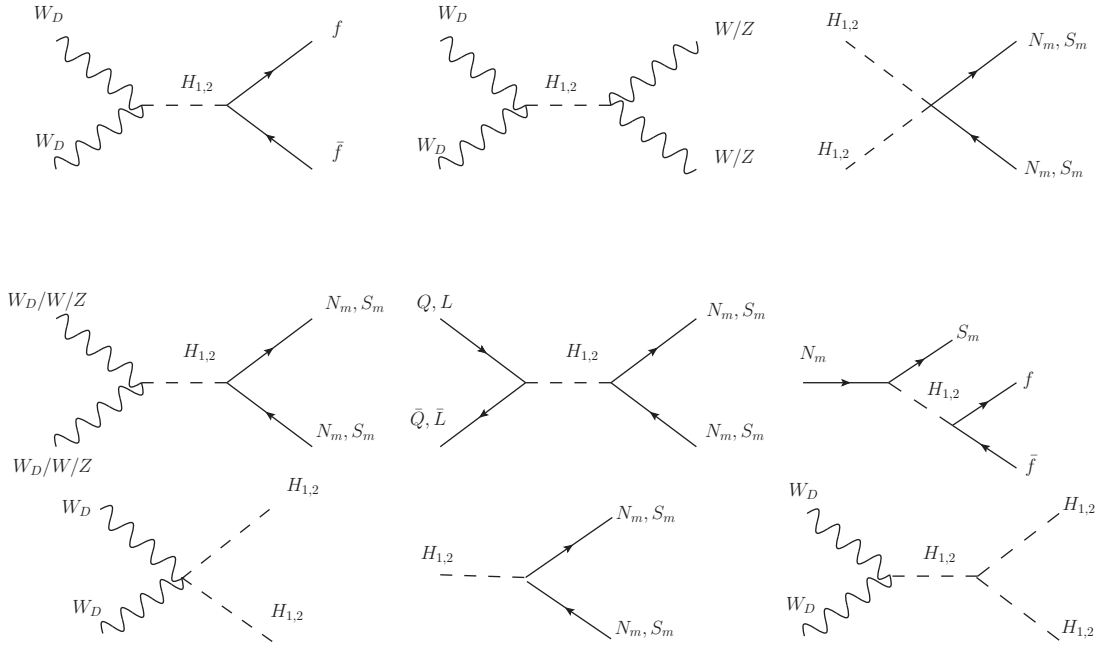
Figure 19. Feynman diagrams relevant for the DM analysis.
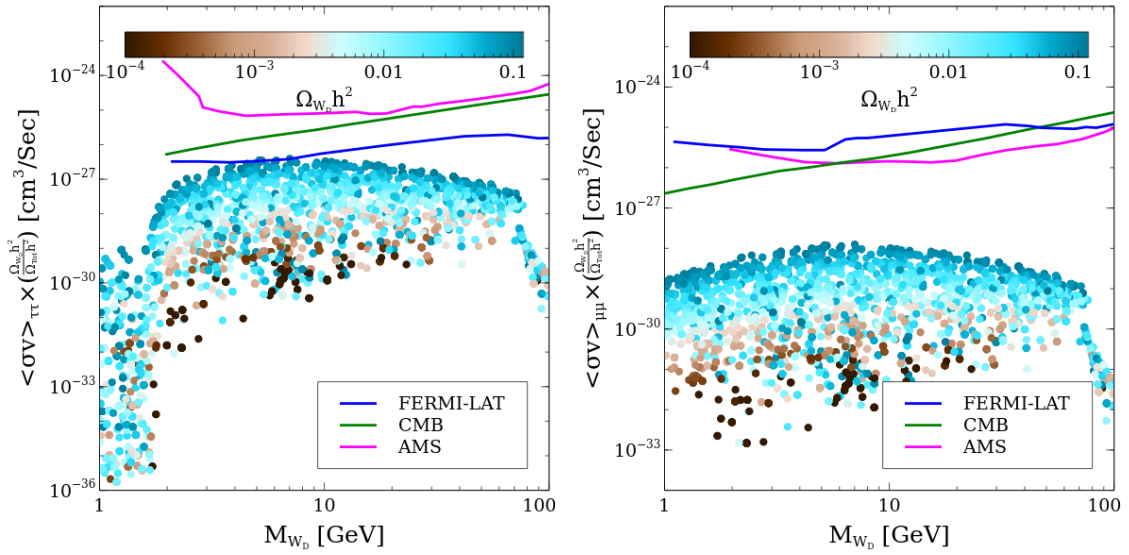

Figure 20. Allowed parameter space satisfying $0.01 \leq \Omega_{\text{DM}}h^2 \leq 0.12$ in the M_{W_D} – $(\Omega_{W_D}/\Omega_{\text{Tot}})\langle\sigma v\rangle_{\tau\tau}$ (left) and M_{W_D} – $(\Omega_{W_D}/\Omega_{\text{Tot}})\langle\sigma v\rangle_{\mu\mu}$ (right) planes. Here, $\Omega_{\text{Tot}}h^2 = 0.12$ is total DM relic density today. Various indirect detection bounds are overlaid with solid lines; see text for detailed explanation. The colour of the points represents the WIMP DM relic density.

E   Field-dependent masses

We summarise the expressions for the field-dependent masses M_i as well as the number of degrees of freedom n_i that appear in the one-loop Coleman-Weinberg potential (5.3):

$$M^2_{H,H_D} = \begin{pmatrix} \mu^2_h + 3\lambda_h \bar{H}^2 + \frac{1}{2}\lambda_{hD}\bar{H}^2_D & \lambda_{hD}\bar{H}\bar{H}_D \\ \lambda_{hD}\bar{H}\bar{H}_D & \mu^2_D + 3\lambda_D \bar{H}^2_D + \frac{1}{2}\lambda_{hD}\bar{H}^2 \end{pmatrix},$$

$$M^2_{W^3,B} = \begin{pmatrix} \frac{1}{4}g^2_2\bar{H}^2 & \frac{1}{4}g_1 g_2\bar{H}^2 \\ \frac{1}{4}g_1 g_2\bar{H}^2 & \frac{1}{4}g^2_1\bar{H}^2 \end{pmatrix},$$

$$M^2_{H^\pm,H^0} = \mu^2_h + \lambda_h \bar{H}^2 + \frac{1}{2}\lambda_{hD}\bar{H}^2_D, \qquad M^2_{H^0_D} = \mu^2_D + \lambda_D \bar{H}^2_D + \frac{1}{2}\lambda_{hD}\bar{H}^2,$$

$$M_{W^{1,2}} = \frac{1}{4}g^2_2\bar{H}^2, \qquad M^2_{Z_D} = g^2_D\bar{H}^2_D, \qquad M^2_t = \frac{1}{2}y^2_t\bar{H}^2,$$

and

$$n_H = n_{H_D} = n_{H^\pm} = n_{H^0} = n_{H^0_D} = 1, \quad n_{W^{1,2,3}} = 6, \quad n_B = 3, \quad n_t = 12, \quad n_{Z_D} = 3.$$

Note that we have considered only the most dominant SM top quark for the fermionic states.

F   Thermal masses

We summarise the expressions for the thermal masses Π_i that enter the one-loop temperature-dependent potential (5.4):

$$\Pi_H = \Pi_{H^\pm,H^0} = \frac{T^2}{48}\left(3g^2_1 + 9g^2_2 + 12y^2_t + 24\lambda_h + 4\lambda_{hD}\right),$$

$$\Pi_{H_D} = \Pi_{H^0_D} = \frac{T^2}{12}\left(3g^2_D + 4\lambda_D + 2\lambda_{hD}\right),$$

$$\Pi_{W^{1,2,3}_L} = \frac{11}{6}g^2_2 T^2, \qquad \Pi_{B_L} = \frac{11}{6}g^2_1 T^2, \qquad \Pi_{Z_{DL}} = \frac{1}{3}g^2_D T^2,$$

where we have considered only the most dominant SM top quark for the fermionic states. Note that fermions and transverse modes of the gauge bosons do not receive any thermal correction.

G   Gravitational wave-related expressions

The quantities $f_{\rm col}$, $f_{\rm sw}$, and $f_{\rm turb}$ that appear in $\Omega_{\rm col}h^2$, $\Omega_{\rm sw}h^2$, and $\Omega_{\rm turb}h^2$ are given as follows [108]:

$$f_{\rm col} = 1.65 \times 10^{-5}\,{\rm Hz}\left(\frac{0.62}{1.8 - 0.1v_w + v^2_w}\right)\left(\frac{\beta}{\mathcal{H}_*}\right)\left(\frac{T_*}{100{\rm GeV}}\right)\left(\frac{g_*}{100}\right)^{\frac{1}{6}},$$

$$f_{\rm sw} = 1.9 \times 10^{-5}\,{\rm Hz}\left(\frac{1}{v_w}\right)\left(\frac{\beta}{\mathcal{H}_*}\right)\left(\frac{T_*}{100{\rm GeV}}\right)\left(\frac{g_*}{100}\right)^{\frac{1}{6}},$$

$$f_{\rm turb} = 2.7 \times 10^{-5}\,{\rm Hz}\left(\frac{1}{v_w}\right)\left(\frac{\beta}{\mathcal{H}_*}\right)\left(\frac{T_*}{100{\rm GeV}}\right)\left(\frac{g_*}{100}\right)^{\frac{1}{6}}.$$

The bubble wall velocity v_w is given by [198]

$$v_w = \frac{\sqrt{1/3} + \sqrt{\alpha^2 + 2\alpha/3}}{1 + \alpha} \,,$$

and we adopt [95]

$$\kappa = \frac{0.715\alpha + (4/27)\sqrt{3\alpha/2}}{1 + 0.715\alpha} \,, \qquad \kappa_v = \frac{\alpha}{0.73 + 0.083\sqrt{\alpha} + \alpha} \,, \qquad \kappa_{\text{turb}} = 0.1\kappa_v \,,$$

References

[1] SUPER-KAMIOKANDE collaboration, *Evidence for oscillation of atmospheric neutrinos*, *Phys. Rev. Lett.* **81** (1998) 1562 [`hep-ex/9807003`] [INSPIRE].

[2] M.C. Gonzalez-Garcia and Y. Nir, *Neutrino Masses and Mixing: Evidence and Implications*, *Rev. Mod. Phys.* **75** (2003) 345 [`hep-ph/0202058`] [INSPIRE].

[3] I. Esteban, M.C. Gonzalez-Garcia, M. Maltoni, T. Schwetz and A. Zhou, *The fate of hints: updated global analysis of three-flavor neutrino oscillations*, *JHEP* **09** (2020) 178 [`arXiv:2007.14792`] [INSPIRE].

[4] PLANCK collaboration, *Planck 2015 results. XIII. Cosmological parameters*, *Astron. Astrophys.* **594** (2016) A13 [`arXiv:1502.01589`] [INSPIRE].

[5] PLANCK collaboration, *Planck 2018 results. VI. Cosmological parameters*, *Astron. Astrophys.* **641** (2020) A6 [`arXiv:1807.06209`] [INSPIRE].

[6] P. Minkowski, $\mu \to e\gamma$ *at a Rate of One Out of* 10^9 *Muon Decays?*, *Phys. Lett. B* **67** (1977) 421 [INSPIRE].

[7] M. Gell-Mann, P. Ramond and R. Slansky, *Complex Spinors and Unified Theories*, *Conf. Proc. C* **790927** (1979) 315 [`arXiv:1306.4669`] [INSPIRE].

[8] S.K. Kang and C.S. Kim, *Extended double seesaw model for neutrino mass spectrum and low scale leptogenesis*, *Phys. Lett. B* **646** (2007) 248 [`hep-ph/0607072`] [INSPIRE].

[9] M. Mitra, G. Senjanovic and F. Vissani, *Neutrinoless Double Beta Decay and Heavy Sterile Neutrinos*, *Nucl. Phys. B* **856** (2012) 26 [`arXiv:1108.0004`] [INSPIRE].

[10] S.K. Majee, M.K. Parida and A. Raychaudhuri, *Neutrino mass and low-scale leptogenesis in a testable SUSY* SO(10) *model*, *Phys. Lett. B* **668** (2008) 299 [`arXiv:0807.3959`] [INSPIRE].

[11] M. Kawasaki, K. Kohri and T. Moroi, *Big-Bang nucleosynthesis and hadronic decay of long-lived massive particles*, *Phys. Rev. D* **71** (2005) 083502 [`astro-ph/0408426`] [INSPIRE].

[12] A. Hook, R. McGehee and H. Murayama, *Cosmologically Viable Low-energy Supersymmetry Breaking*, *Phys. Rev. D* **98** (2018) 115036 [`arXiv:1801.10160`] [INSPIRE].

[13] J.P. Ostriker and P.J.E. Peebles, *A Numerical Study of the Stability of Flattened Galaxies: or, can Cold Galaxies Survive?*, *Astrophys. J.* **186** (1973) 467 [INSPIRE].

[14] E. Corbelli and P. Salucci, *The Extended Rotation Curve and the Dark Matter Halo of M33*, *Mon. Not. Roy. Astron. Soc.* **311** (2000) 441 [astro-ph/9909252] [InSPIRE].

[15] J.E. Gunn, B.W. Lee, I. Lerche, D.N. Schramm and G. Steigman, *Some Astrophysical Consequences of the Existence of a Heavy Stable Neutral Lepton*, *Astrophys. J.* **223** (1978) 1015 [InSPIRE].

[16] P. Hut, *Limits on Masses and Number of Neutral Weakly Interacting Particles*, *Phys. Lett. B* **69** (1977) 85 [InSPIRE].

[17] B.W. Lee and S. Weinberg, *Cosmological Lower Bound on Heavy Neutrino Masses*, *Phys. Rev. Lett.* **39** (1977) 165 [InSPIRE].

[18] G. Bertone, D. Hooper and J. Silk, *Particle dark matter: Evidence, candidates and constraints*, *Phys. Rept.* **405** (2005) 279 [hep-ph/0404175] [InSPIRE].

[19] XENON collaboration, *Dark Matter Search Results from a One Ton-Year Exposure of XENON1T*, *Phys. Rev. Lett.* **121** (2018) 111302 [arXiv:1805.12562] [InSPIRE].

[20] CMS collaboration, *Phenomenological MSSM interpretation of CMS searches in pp collisions at $\sqrt{s} = 7$ and 8 TeV*, *JHEP* **10** (2016) 129 [arXiv:1606.03577] [InSPIRE].

[21] MAGIC and FERMI-LAT collaborations, *Limits to Dark Matter Annihilation Cross-Section from a Combined Analysis of MAGIC and Fermi-LAT Observations of Dwarf Satellite Galaxies*, *JCAP* **02** (2016) 039 [arXiv:1601.06590] [InSPIRE].

[22] G. Arcadi et al., *The waning of the WIMP? A review of models, searches, and constraints*, *Eur. Phys. J. C* **78** (2018) 203 [arXiv:1703.07364] [InSPIRE].

[23] PANDAX-II collaboration, *Dark Matter Results from First 98.7 Days of Data from the PandaX-II Experiment*, *Phys. Rev. Lett.* **117** (2016) 121303 [arXiv:1607.07400] [InSPIRE].

[24] LUX collaboration, *Results from a search for dark matter in the complete LUX exposure*, *Phys. Rev. Lett.* **118** (2017) 021303 [arXiv:1608.07648] [InSPIRE].

[25] J. McDonald, *Thermally generated gauge singlet scalars as selfinteracting dark matter*, *Phys. Rev. Lett.* **88** (2002) 091304 [hep-ph/0106249] [InSPIRE].

[26] K.-Y. Choi and L. Roszkowski, *E-WIMPs*, *AIP Conf. Proc.* **805** (2005) 30 [hep-ph/0511003] [InSPIRE].

[27] A. Kusenko, *Sterile neutrinos, dark matter, and the pulsar velocities in models with a Higgs singlet*, *Phys. Rev. Lett.* **97** (2006) 241301 [hep-ph/0609081] [InSPIRE].

[28] L.J. Hall, K. Jedamzik, J. March-Russell and S.M. West, *Freeze-In Production of FIMP Dark Matter*, *JHEP* **03** (2010) 080 [arXiv:0911.1120] [InSPIRE].

[29] C. Cheung, G. Elor and L. Hall, *Gravitino Freeze-In*, *Phys. Rev. D* **84** (2011) 115021 [arXiv:1103.4394] [InSPIRE].

[30] F. Elahi, C. Kolda and J. Unwin, *UltraViolet Freeze-in*, *JHEP* **03** (2015) 048 [arXiv:1410.6157] [InSPIRE].

[31] G. Arcadi, L. Covi and M. Nardecchia, *Gravitino Dark Matter and low-scale Baryogenesis*, *Phys. Rev. D* **92** (2015) 115006 [arXiv:1507.05584] [InSPIRE].

[32] N. Bernal, M. Heikinheimo, T. Tenkanen, K. Tuominen and V. Vaskonen, *The Dawn of FIMP Dark Matter: A Review of Models and Constraints*, *Int. J. Mod. Phys. A* **32** (2017) 1730023 [arXiv:1706.07442] [InSPIRE].

[33] K. Benakli, Y. Chen, E. Dudas and Y. Mambrini, *Minimal model of gravitino dark matter*, *Phys. Rev. D* **95** (2017) 095002 [arXiv:1701.06574] [InSPIRE].

[34] N. Bernal, M. Dutra, Y. Mambrini, K. Olive, M. Peloso and M. Pierre, *Spin-2 Portal Dark Matter*, *Phys. Rev. D* **97** (2018) 115020 [`arXiv:1803.01866`] [InSPIRE].

[35] N. Bernal, F. Elahi, C. Maldonado and J. Unwin, *Ultraviolet Freeze-in and Non-Standard Cosmologies*, *JCAP* **11** (2019) 026 [`arXiv:1909.07992`] [InSPIRE].

[36] B. Barman, S. Bhattacharya and M. Zakeri, *Non-Abelian Vector Boson as FIMP Dark Matter*, *JCAP* **02** (2020) 029 [`arXiv:1905.07236`] [InSPIRE].

[37] L. Covi, A. Ghosh, T. Mondal and B. Mukhopadhyaya, *Models of decaying FIMP Dark Matter: potential links with the Neutrino Sector*, `arXiv:2008.12550` [InSPIRE].

[38] S. Khan, *Explaining Xenon-1T signal with FIMP dark matter and neutrino mass in a* $U(1)_X$ *extension*, *Eur. Phys. J. C* **81** (2021) 598 [`arXiv:2007.13008`] [InSPIRE].

[39] M.A.G. Garcia, Y. Mambrini, K.A. Olive and S. Verner, *Case for decaying spin-3/2 dark matter*, *Phys. Rev. D* **102** (2020) 083533 [`arXiv:2006.03325`] [InSPIRE].

[40] N. Bernal, J. Rubio and H. Veermäe, *UV Freeze-in in Starobinsky Inflation*, *JCAP* **10** (2020) 021 [`arXiv:2006.02442`] [InSPIRE].

[41] B. Barman, D. Borah and R. Roshan, *Effective Theory of Freeze-in Dark Matter*, *JCAP* **11** (2020) 021 [`arXiv:2007.08768`] [InSPIRE].

[42] B. Barman, S. Bhattacharya and B. Grzadkowski, *Feebly coupled vector boson dark matter in effective theory*, *JHEP* **12** (2020) 162 [`arXiv:2009.07438`] [InSPIRE].

[43] B. Barman, P. Ghosh, A. Ghoshal and L. Mukherjee, *Shedding flavor on dark via freeze-in:* $U(1)_{B-3Li}$ *gauged extensions*, *JCAP* **08** (2022) 049 [`arXiv:2112.12798`] [InSPIRE].

[44] B. Barman and A. Ghoshal, *Scale invariant FIMP miracle*, *JCAP* **03** (2022) 003 [`arXiv:2109.03259`] [InSPIRE].

[45] G. Bélanger, S. Khan, R. Padhan, M. Mitra and S. Shil, *Right handed neutrinos, TeV scale BSM neutral Higgs boson, and FIMP dark matter in an EFT framework*, *Phys. Rev. D* **104** (2021) 055047 [`arXiv:2104.04373`] [InSPIRE].

[46] B. Barman and A. Ghoshal, *Probing pre-BBN era with scale invariant FIMP*, *JCAP* **10** (2022) 082 [`arXiv:2203.13269`] [InSPIRE].

[47] K. Choi and S.H. Im, *Realizing the relaxion from multiple axions and its UV completion with high scale supersymmetry*, *JHEP* **01** (2016) 149 [`arXiv:1511.00132`] [InSPIRE].

[48] D.E. Kaplan and R. Rattazzi, *Large field excursions and approximate discrete symmetries from a clockwork axion*, *Phys. Rev. D* **93** (2016) 085007 [`arXiv:1511.01827`] [InSPIRE].

[49] G.F. Giudice and M. McCullough, *A Clockwork Theory*, *JHEP* **02** (2017) 036 [`arXiv:1610.07962`] [InSPIRE].

[50] J. Kim and J. McDonald, *Clockwork Higgs portal model for freeze-in dark matter*, *Phys. Rev. D* **98** (2018) 023533 [`arXiv:1709.04105`] [InSPIRE].

[51] J. Kim and J. Mcdonald, *Freeze-In Dark Matter from a sub-Higgs Mass Clockwork Sector via the Higgs Portal*, *Phys. Rev. D* **98** (2018) 123503 [`arXiv:1804.02661`] [InSPIRE].

[52] A. Goudelis, K.A. Mohan and D. Sengupta, *Clockworking FIMPs*, *JHEP* **10** (2018) 014 [`arXiv:1807.06642`] [InSPIRE].

[53] K.M. Zurek, *Multi-Component Dark Matter*, *Phys. Rev. D* **79** (2009) 115002 [`arXiv:0811.4429`] [InSPIRE].

[54] S. Profumo, K. Sigurdson and L. Ubaldi, *Can we discover multi-component WIMP dark matter?*, *JCAP* **12** (2009) 016 [arXiv:0907.4374] [INSPIRE].

[55] D. Feldman, Z. Liu, P. Nath and G. Peim, *Multicomponent Dark Matter in Supersymmetric Hidden Sector Extensions*, *Phys. Rev. D* **81** (2010) 095017 [arXiv:1004.0649] [INSPIRE].

[56] P. Ko and Y. Omura, *Supersymmetric* U(1)B × U(1)L *model with leptophilic and leptophobic cold dark matters*, *Phys. Lett. B* **701** (2011) 363 [arXiv:1012.4679] [INSPIRE].

[57] A. Drozd, B. Grzadkowski and J. Wudka, *Multi-Scalar-Singlet Extension of the Standard Model — the Case for Dark Matter and an Invisible Higgs Boson*, *JHEP* **04** (2012) 006 [arXiv:1112.2582] [INSPIRE].

[58] M. Aoki, M. Duerr, J. Kubo and H. Takano, *Multi-Component Dark Matter Systems and Their Observation Prospects*, *Phys. Rev. D* **86** (2012) 076015 [arXiv:1207.3318] [INSPIRE].

[59] S. Bhattacharya, A. Drozd, B. Grzadkowski and J. Wudka, *Two-Component Dark Matter*, *JHEP* **10** (2013) 158 [arXiv:1309.2986] [INSPIRE].

[60] S. Baek, P. Ko and W.-I. Park, *Hidden sector monopole, vector dark matter and dark radiation with Higgs portal*, *JCAP* **10** (2014) 067 [arXiv:1311.1035] [INSPIRE].

[61] S. Esch, M. Klasen and C.E. Yaguna, *A minimal model for two-component dark matter*, *JHEP* **09** (2014) 108 [arXiv:1406.0617] [INSPIRE].

[62] P. Ko and Y. Tang, *νΛMDM: A model for sterile neutrino and dark matter reconciles cosmological and neutrino oscillation data after BICEP2*, *Phys. Lett. B* **739** (2014) 62 [arXiv:1404.0236] [INSPIRE].

[63] L. Bian, T. Li, J. Shu and X.-C. Wang, *Two component dark matter with multi-Higgs portals*, *JHEP* **03** (2015) 126 [arXiv:1412.5443] [INSPIRE].

[64] A. Karam and K. Tamvakis, *Dark matter and neutrino masses from a scale-invariant multi-Higgs portal*, *Phys. Rev. D* **92** (2015) 075010 [arXiv:1508.03031] [INSPIRE].

[65] G. Arcadi, C. Gross, O. Lebedev, Y. Mambrini, S. Pokorski and T. Toma, *Multicomponent Dark Matter from Gauge Symmetry*, *JHEP* **12** (2016) 081 [arXiv:1611.00365] [INSPIRE].

[66] A. Dutta Banik, M. Pandey, D. Majumdar and A. Biswas, *Two component WIMP-FImP dark matter model with singlet fermion, scalar and pseudo scalar*, *Eur. Phys. J. C* **77** (2017) 657 [arXiv:1612.08621] [INSPIRE].

[67] A. Karam and K. Tamvakis, *Dark Matter from a Classically Scale-Invariant* SU(3)X, *Phys. Rev. D* **94** (2016) 055004 [arXiv:1607.01001] [INSPIRE].

[68] S. Bhattacharya, P. Poulose and P. Ghosh, *Multipartite Interacting Scalar Dark Matter in the light of updated LUX data*, *JCAP* **04** (2017) 043 [arXiv:1607.08461] [INSPIRE].

[69] P. Ko and Y. Tang, *Residual Non-Abelian Dark Matter and Dark Radiation*, *Phys. Lett. B* **768** (2017) 12 [arXiv:1609.02307] [INSPIRE].

[70] M. Aoki and T. Toma, *Implications of Two-component Dark Matter Induced by Forbidden Channels and Thermal Freeze-out*, *JCAP* **01** (2017) 042 [arXiv:1611.06746] [INSPIRE].

[71] A. Ahmed, M. Duch, B. Grzadkowski and M. Iglicki, *Multi-Component Dark Matter: the vector and fermion case*, *Eur. Phys. J. C* **78** (2018) 905 [arXiv:1710.01853] [INSPIRE].

[72] M. Aoki and T. Toma, *Boosted Self-interacting Dark Matter in a Multi-component Dark Matter Model*, *JCAP* **10** (2018) 020 [arXiv:1806.09154] [INSPIRE].

[73] S. Chakraborti and P. Poulose, *Interplay of Scalar and Fermionic Components in a Multi-component Dark Matter Scenario*, *Eur. Phys. J. C* **79** (2019) 420 [arXiv:1808.01979] [INSPIRE].

[74] A. Poulin and S. Godfrey, *Multicomponent dark matter from a hidden gauged* SU(3), *Phys. Rev. D* **99** (2019) 076008 [arXiv:1808.04901] [INSPIRE].

[75] S. Yaser Ayazi and A. Mohamadnejad, *Scale-Invariant Two Component Dark Matter*, *Eur. Phys. J. C* **79** (2019) 140 [arXiv:1808.08706] [INSPIRE].

[76] S. Chakraborti, A. Dutta Banik and R. Islam, *Probing Multicomponent Extension of Inert Doublet Model with a Vector Dark Matter*, *Eur. Phys. J. C* **79** (2019) 662 [arXiv:1810.05595] [INSPIRE].

[77] S. Bhattacharya, P. Ghosh, A.K. Saha and A. Sil, *Two component dark matter with inert Higgs doublet: neutrino mass, high scale validity and collider searches*, *JHEP* **03** (2020) 090 [arXiv:1905.12583] [INSPIRE].

[78] C.-R. Chen, Y.-X. Lin, C.S. Nugroho, R. Ramos, Y.-L.S. Tsai and T.-C. Yuan, *Complex scalar dark matter in the gauged two-Higgs-doublet model*, *Phys. Rev. D* **101** (2020) 035037 [arXiv:1910.13138] [INSPIRE].

[79] C.E. Yaguna and O. Zapata, *Multi-component scalar dark matter from a Z_N symmetry: a systematic analysis*, *JHEP* **03** (2020) 109 [arXiv:1911.05515] [INSPIRE].

[80] S. Bhattacharya, N. Chakrabarty, R. Roshan and A. Sil, *Multicomponent dark matter in extended* U(1)$_{B-L}$: *neutrino mass and high scale validity*, *JCAP* **04** (2020) 013 [arXiv:1910.00612] [INSPIRE].

[81] A. Betancur, G. Palacio and A. Rivera, *Inert doublet as multicomponent dark matter*, *Nucl. Phys. B* **962** (2021) 115276 [arXiv:2002.02036] [INSPIRE].

[82] G. Bélanger, A. Pukhov, C.E. Yaguna and O. Zapata, *The Z_5 model of two-component dark matter*, *JHEP* **09** (2020) 030 [arXiv:2006.14922] [INSPIRE].

[83] G. Bélanger, A. Mjallal and A. Pukhov, *Two dark matter candidates: The case of inert doublet and singlet scalars*, *Phys. Rev. D* **105** (2022) 035018 [arXiv:2108.08061] [INSPIRE].

[84] S. Bhattacharya, S. Chakraborti and D. Pradhan, *Electroweak symmetry breaking and WIMP-FIMP dark matter*, *JHEP* **07** (2022) 091 [arXiv:2110.06985] [INSPIRE].

[85] P. Das, M.K. Das and N. Khan, *The FIMP-WIMP dark matter in the extended singlet scalar model*, *Nucl. Phys. B* **975** (2022) 115677 [arXiv:2104.03271] [INSPIRE].

[86] A. Betancur, A. Castillo, G. Palacio and J. Suarez, *Multicomponent scalar dark matter at high-intensity proton beam experiments*, *J. Phys. G* **49** (2022) 075003 [arXiv:2109.11586] [INSPIRE].

[87] N. Chakrabarty, R. Roshan and A. Sil, *Two-component doublet-triplet scalar dark matter stabilizing the electroweak vacuum*, *Phys. Rev. D* **105** (2022) 115010 [arXiv:2102.06032] [INSPIRE].

[88] A. Mohamadnejad, *Electroweak phase transition and gravitational waves in a two-component dark matter model*, *JHEP* **03** (2022) 188 [arXiv:2111.04342] [INSPIRE].

[89] B. Díaz Sáez, K. Möhling and D. Stöckinger, *Two real scalar WIMP model in the assisted freeze-out scenario*, *JCAP* **10** (2021) 027 [arXiv:2103.17064] [INSPIRE].

[90] S.-M. Choi, J. Kim, P. Ko and J. Li, *A multi-component SIMP model with* U(1)$_X \to Z_2 \times Z_3$, *JHEP* **09** (2021) 028 [arXiv:2103.05956] [INSPIRE].

[91] G. Bélanger, A. Mjallal and A. Pukhov, *WIMP and FIMP dark matter in the inert doublet plus singlet model*, *Phys. Rev. D* **106** (2022) 095019 [`arXiv:2205.04101`] [InSPIRE].

[92] A. Das, S. Gola, S. Mandal and N. Sinha, *Two-component scalar and fermionic dark matter candidates in a generic* U(1)X *model*, *Phys. Lett. B* **829** (2022) 137117 [`arXiv:2202.01443`] [InSPIRE].

[93] S.-Y. Ho, P. Ko and C.-T. Lu, *Scalar and fermion two-component SIMP dark matter with an accidental* Z_4 *symmetry*, *JHEP* **03** (2022) 005 [`arXiv:2201.06856`] [InSPIRE].

[94] F. Costa, S. Khan and J. Kim, *A two-component dark matter model and its associated gravitational waves*, *JHEP* **06** (2022) 026 [`arXiv:2202.13126`] [InSPIRE].

[95] M. Kamionkowski, A. Kosowsky and M.S. Turner, *Gravitational radiation from first order phase transitions*, *Phys. Rev. D* **49** (1994) 2837 [`astro-ph/9310044`] [InSPIRE].

[96] J. Baker et al., *The Laser Interferometer Space Antenna: Unveiling the Millihertz Gravitational Wave Sky*, `arXiv:1907.06482` [InSPIRE].

[97] N. Seto, S. Kawamura and T. Nakamura, *Possibility of direct measurement of the acceleration of the universe using 0.1-Hz band laser interferometer gravitational wave antenna in space*, *Phys. Rev. Lett.* **87** (2001) 221103 [`astro-ph/0108011`] [InSPIRE].

[98] S. Kawamura et al., *The Japanese space gravitational wave antenna DECIGO*, *Class. Quant. Grav.* **23** (2006) S125 [InSPIRE].

[99] S. Sato et al., *The status of DECIGO*, *J. Phys. Conf. Ser.* **840** (2017) 012010 [InSPIRE].

[100] S. Isoyama, H. Nakano and T. Nakamura, *Multiband Gravitational-Wave Astronomy: Observing binary inspirals with a decihertz detector, B-DECIGO*, *PTEP* **2018** (2018) 073E01 [`arXiv:1802.06977`] [InSPIRE].

[101] S. Kawamura et al., *Current status of space gravitational wave antenna DECIGO and B-DECIGO*, *PTEP* **2021** (2021) 05A105 [`arXiv:2006.13545`] [InSPIRE].

[102] V. Corbin and N.J. Cornish, *Detecting the cosmic gravitational wave background with the big bang observer*, *Class. Quant. Grav.* **23** (2006) 2435 [`gr-qc/0512039`] [InSPIRE].

[103] J. Crowder and N.J. Cornish, *Beyond LISA: Exploring future gravitational wave missions*, *Phys. Rev. D* **72** (2005) 083005 [`gr-qc/0506015`] [InSPIRE].

[104] G.M. Harry, P. Fritschel, D.A. Shaddock, W. Folkner and E.S. Phinney, *Laser interferometry for the big bang observer*, *Class. Quant. Grav.* **23** (2006) 4887 [InSPIRE].

[105] C. Grojean and G. Servant, *Gravitational Waves from Phase Transitions at the Electroweak Scale and Beyond*, *Phys. Rev. D* **75** (2007) 043507 [`hep-ph/0607107`] [InSPIRE].

[106] S.J. Huber and T. Konstandin, *Gravitational Wave Production by Collisions: More Bubbles*, *JCAP* **09** (2008) 022 [`arXiv:0806.1828`] [InSPIRE].

[107] J.R. Espinosa, T. Konstandin, J.M. No and M. Quiros, *Some Cosmological Implications of Hidden Sectors*, *Phys. Rev. D* **78** (2008) 123528 [`arXiv:0809.3215`] [InSPIRE].

[108] C. Caprini et al., *Science with the space-based interferometer eLISA. II: Gravitational waves from cosmological phase transitions*, *JCAP* **04** (2016) 001 [`arXiv:1512.06239`] [InSPIRE].

[109] M. Artymowski, M. Lewicki and J.D. Wells, *Gravitational wave and collider implications of electroweak baryogenesis aided by non-standard cosmology*, *JHEP* **03** (2017) 066 [`arXiv:1609.07143`] [InSPIRE].

[110] I. Baldes, *Gravitational waves from the asymmetric-dark-matter generating phase transition*, *JCAP* **05** (2017) 028 [`arXiv:1702.02117`] [InSPIRE].

[111] A. Beniwal, M. Lewicki, M. White and A.G. Williams, *Gravitational waves and electroweak baryogenesis in a global study of the extended scalar singlet model*, *JHEP* **02** (2019) 183 [arXiv:1810.02380] [INSPIRE].

[112] K. Hashino, M. Kakizaki, S. Kanemura, P. Ko and T. Matsui, *Gravitational waves from first order electroweak phase transition in models with the* $U(1)_X$ *gauge symmetry*, *JHEP* **06** (2018) 088 [arXiv:1802.02947] [INSPIRE].

[113] C. Caprini and D.G. Figueroa, *Cosmological Backgrounds of Gravitational Waves*, *Class. Quant. Grav.* **35** (2018) 163001 [arXiv:1801.04268] [INSPIRE].

[114] L. Bian and Y.-L. Tang, *Thermally modified sterile neutrino portal dark matter and gravitational waves from phase transition: The Freeze-in case*, *JHEP* **12** (2018) 006 [arXiv:1810.03172] [INSPIRE].

[115] L. Bian and X. Liu, *Two-step strongly first-order electroweak phase transition modified FIMP dark matter, gravitational wave signals, and the neutrino mass*, *Phys. Rev. D* **99** (2019) 055003 [arXiv:1811.03279] [INSPIRE].

[116] L. Bian, W. Cheng, H.-K. Guo and Y. Zhang, *Cosmological implications of a* $B − L$ *charged hidden scalar: leptogenesis and gravitational waves*, *Chin. Phys. C* **45** (2021) 113104 [arXiv:1907.13589] [INSPIRE].

[117] L. Bian, Y. Wu and K.-P. Xie, *Electroweak phase transition with composite Higgs models: calculability, gravitational waves and collider searches*, *JHEP* **12** (2019) 028 [arXiv:1909.02014] [INSPIRE].

[118] C. Caprini et al., *Detecting gravitational waves from cosmological phase transitions with LISA: an update*, *JCAP* **03** (2020) 024 [arXiv:1910.13125] [INSPIRE].

[119] Y. Di, J. Wang, R. Zhou, L. Bian, R.-G. Cai and J. Liu, *Magnetic Field and Gravitational Waves from the First-Order Phase Transition*, *Phys. Rev. Lett.* **126** (2021) 251102 [arXiv:2012.15625] [INSPIRE].

[120] R. Zhou, L. Bian and J. Shu, *Probing new physics for* $(g − 2)_\mu$ *and gravitational waves*, arXiv:2104.03519 [INSPIRE].

[121] L. Bian, Y.-L. Tang and R. Zhou, *FIMP dark matter mediated by a massive gauge boson around the phase transition period and the gravitational waves production*, *Phys. Rev. D* **106** (2022) 035028 [arXiv:2111.10608] [INSPIRE].

[122] W. Altmannshofer, S. Gori, J. Martín-Albo, A. Sousa and M. Wallbank, *Neutrino Tridents at DUNE*, *Phys. Rev. D* **100** (2019) 115029 [arXiv:1902.06765] [INSPIRE].

[123] A. Biswas and S. Khan, $(g − 2)_{e,\mu}$ *and strongly interacting dark matter with collider implications*, *JHEP* **07** (2022) 037 [arXiv:2112.08393] [INSPIRE].

[124] M. Bauer, P. Foldenauer and J. Jaeckel, *Hunting All the Hidden Photons*, *JHEP* **07** (2018) 094 [arXiv:1803.05466] [INSPIRE].

[125] FERMI-LAT collaboration, *Updated search for spectral lines from Galactic dark matter interactions with pass 8 data from the Fermi Large Area Telescope*, *Phys. Rev. D* **91** (2015) 122002 [arXiv:1506.00013] [INSPIRE].

[126] B. Pontecorvo, *Inverse beta processes and nonconservation of lepton charge*, *Zh. Eksp. Teor. Fiz.* **34** (1957) 247 [INSPIRE].

[127] Z. Maki, M. Nakagawa and S. Sakata, *Remarks on the unified model of elementary particles*, *Prog. Theor. Phys.* **28** (1962) 870 [INSPIRE].

[128] MEG collaboration, *Search for the lepton flavour violating decay* $\mu^+ \to e^+\gamma$ *with the full dataset of the MEG experiment*, *Eur. Phys. J. C* **76** (2016) 434 [arXiv:1605.05081] [INSPIRE].

[129] SINDRUM collaboration, *Search for the Decay* $\mu^+ \to e^+e^+e^-$, *Nucl. Phys. B* **299** (1988) 1 [INSPIRE].

[130] P. Wintz, *Results of the SINDRUM-II experiment*, *Conf. Proc. C* **980420** (1998) 534 [INSPIRE].

[131] A. Ilakovac and A. Pilaftsis, *Flavor violating charged lepton decays in seesaw-type models*, *Nucl. Phys. B* **437** (1995) 491 [hep-ph/9403398] [INSPIRE].

[132] M. Lindner, M. Platscher and F.S. Queiroz, *A Call for New Physics: The Muon Anomalous Magnetic Moment and Lepton Flavor Violation*, *Phys. Rept.* **731** (2018) 1 [arXiv:1610.06587] [INSPIRE].

[133] CHARM collaboration, *A Search for Decays of Heavy Neutrinos in the Mass Range 0.5-GeV to 2.8-GeV*, *Phys. Lett. B* **166** (1986) 473 [INSPIRE].

[134] CHARM II collaboration, *Search for heavy isosinglet neutrinos*, *Phys. Lett. B* **343** (1995) 453 [INSPIRE].

[135] BELLE collaboration, *Search for heavy neutrinos at Belle*, *Phys. Rev. D* **87** (2013) 071102 [arXiv:1301.1105] [INSPIRE].

[136] DELPHI collaboration, *Search for neutral heavy leptons produced in Z decays*, *Z. Phys. C* **74** (1997) 57 [INSPIRE].

[137] I. Krasnov, *DUNE prospects in the search for sterile neutrinos*, *Phys. Rev. D* **100** (2019) 075023 [arXiv:1902.06099] [INSPIRE].

[138] P. Ballett, T. Boschi and S. Pascoli, *Heavy Neutral Leptons from low-scale seesaws at the DUNE Near Detector*, *JHEP* **03** (2020) 111 [arXiv:1905.00284] [INSPIRE].

[139] SHiP collaboration, *Sensitivity of the SHiP experiment to Heavy Neutral Leptons*, *JHEP* **04** (2019) 077 [arXiv:1811.00930] [INSPIRE].

[140] J.P. Chou, D. Curtin and H.J. Lubatti, *New Detectors to Explore the Lifetime Frontier*, *Phys. Lett. B* **767** (2017) 29 [arXiv:1606.06298] [INSPIRE].

[141] E.J. Chun, A. Das, S. Mandal, M. Mitra and N. Sinha, *Sensitivity of Lepton Number Violating Meson Decays in Different Experiments*, *Phys. Rev. D* **100** (2019) 095022 [arXiv:1908.09562] [INSPIRE].

[142] FCC-EE STUDY TEAM collaboration, *Search for Heavy Right Handed Neutrinos at the FCC-ee*, *Nucl. Part. Phys. Proc.* **273-275** (2016) 1883 [arXiv:1411.5230] [INSPIRE].

[143] A. Blondel et al., *Searches for long-lived particles at the future FCC-ee*, *Front. in Phys.* **10** (2022) 967881 [arXiv:2203.05502] [INSPIRE].

[144] M. Drewes and J. Hajer, *Heavy Neutrinos in displaced vertex searches at the LHC and HL-LHC*, *JHEP* **02** (2020) 070 [arXiv:1903.06100] [INSPIRE].

[145] S. Antusch, E. Cazzato and O. Fischer, *Sterile neutrino searches via displaced vertices at LHCb*, *Phys. Lett. B* **774** (2017) 114 [arXiv:1706.05990] [INSPIRE].

[146] NuTeV and E815 collaborations, *Search for neutral heavy leptons in a high-energy neutrino beam*, *Phys. Rev. Lett.* **83** (1999) 4943 [hep-ex/9908011] [INSPIRE].

[147] FMMF collaboration, *Search for neutral weakly interacting massive particles in the Fermilab Tevatron wide band neutrino beam*, *Phys. Rev. D* **52** (1995) 6 [INSPIRE].

[148] J.L. Feng, I. Galon, F. Kling and S. Trojanowski, *ForwArd Search ExpeRiment at the LHC*, *Phys. Rev. D* **97** (2018) 035001 [arXiv:1708.09389] [InSPIRE].

[149] D. Dercks, H.K. Dreiner, M. Hirsch and Z.S. Wang, *Long-Lived Fermions at AL3X*, *Phys. Rev. D* **99** (2019) 055020 [arXiv:1811.01995] [InSPIRE].

[150] A. Alloul, N.D. Christensen, C. Degrande, C. Duhr and B. Fuks, *FeynRules 2.0 — A complete toolbox for tree-level phenomenology*, *Comput. Phys. Commun.* **185** (2014) 2250 [arXiv:1310.1921] [InSPIRE].

[151] A. Belyaev, N.D. Christensen and A. Pukhov, *CalcHEP 3.4 for collider physics within and beyond the Standard Model*, *Comput. Phys. Commun.* **184** (2013) 1729 [arXiv:1207.6082] [InSPIRE].

[152] G. Bélanger, F. Boudjema, A. Pukhov and A. Semenov, *MicrOMEGAs 2.0: A program to calculate the relic density of dark matter in a generic model*, *Comput. Phys. Commun.* **176** (2007) 367 [hep-ph/0607059] [InSPIRE].

[153] M. Carena, Z. Liu and Y. Wang, *Electroweak phase transition with spontaneous Z_2-breaking*, *JHEP* **08** (2020) 107 [arXiv:1911.10206] [InSPIRE].

[154] CMS collaboration, *Combined measurements of Higgs boson couplings in proton-proton collisions at $\sqrt{s} = 13\,TeV$*, *Eur. Phys. J. C* **79** (2019) 421 [arXiv:1809.10733] [InSPIRE].

[155] ATLAS and CMS collaborations, *Measurements of the Higgs boson production and decay rates and constraints on its couplings from a combined ATLAS and CMS analysis of the LHC pp collision data at $\sqrt{s} = 7$ and 8 TeV*, *JHEP* **08** (2016) 045 [arXiv:1606.02266] [InSPIRE].

[156] A. Berlin, D. Hooper and S.D. McDermott, *Simplified Dark Matter Models for the Galactic Center Gamma-Ray Excess*, *Phys. Rev. D* **89** (2014) 115022 [arXiv:1404.0022] [InSPIRE].

[157] P. Junnarkar and A. Walker-Loud, *Scalar strange content of the nucleon from lattice QCD*, *Phys. Rev. D* **87** (2013) 114510 [arXiv:1301.1114] [InSPIRE].

[158] LZ collaboration, *First Dark Matter Search Results from the LUX-ZEPLIN (LZ) Experiment*, arXiv:2207.03764 [InSPIRE].

[159] PandaX-II collaboration, *Dark Matter Results From 54-Ton-Day Exposure of PandaX-II Experiment*, *Phys. Rev. Lett.* **119** (2017) 181302 [arXiv:1708.06917] [InSPIRE].

[160] PandaX collaboration, *The first results of PandaX-4T*, *Int. J. Mod. Phys. D* **31** (2022) 2230007 [InSPIRE].

[161] DarkSide collaboration, *DarkSide-50 532-day Dark Matter Search with Low-Radioactivity Argon*, *Phys. Rev. D* **98** (2018) 102006 [arXiv:1802.07198] [InSPIRE].

[162] DarkSide collaboration, *Low-Mass Dark Matter Search with the DarkSide-50 Experiment*, *Phys. Rev. Lett.* **121** (2018) 081307 [arXiv:1802.06994] [InSPIRE].

[163] M. Ibe, W. Nakano, Y. Shoji and K. Suzuki, *Migdal Effect in Dark Matter Direct Detection Experiments*, *JHEP* **03** (2018) 194 [arXiv:1707.07258] [InSPIRE].

[164] SuperCDMS collaboration, *Search for Low-Mass Dark Matter with CDMSlite Using a Profile Likelihood Fit*, *Phys. Rev. D* **99** (2019) 062001 [arXiv:1808.09098] [InSPIRE].

[165] CRESST collaboration, *Results on MeV-scale dark matter from a gram-scale cryogenic calorimeter operated above ground*, *Eur. Phys. J. C* **77** (2017) 637 [arXiv:1707.06749] [InSPIRE].

[166] CRESST collaboration, *First results from the CRESST-III low-mass dark matter program*, *Phys. Rev. D* **100** (2019) 102002 [arXiv:1904.00498] [InSPIRE].

[167] FERMI-LAT collaboration, *Searching for Dark Matter Annihilation from Milky Way Dwarf Spheroidal Galaxies with Six Years of Fermi Large Area Telescope Data*, *Phys. Rev. Lett.* **115** (2015) 231301 [arXiv:1503.02641] [INSPIRE].

[168] R.K. Leane, T.R. Slatyer, J.F. Beacom and K.C.Y. Ng, *GeV-scale thermal WIMPs: Not even slightly ruled out*, *Phys. Rev. D* **98** (2018) 023016 [arXiv:1805.10305] [INSPIRE].

[169] L. Bergstrom, T. Bringmann, I. Cholis, D. Hooper and C. Weniger, *New Limits on Dark Matter Annihilation from AMS Cosmic Ray Positron Data*, *Phys. Rev. Lett.* **111** (2013) 171101 [arXiv:1306.3983] [INSPIRE].

[170] ATLAS collaboration, *Combination of searches for invisible Higgs boson decays with the ATLAS experiment*, *Phys. Rev. Lett.* **122** (2019) 231801 [arXiv:1904.05105] [INSPIRE].

[171] L. Covi, J.E. Kim and L. Roszkowski, *Axinos as cold dark matter*, *Phys. Rev. Lett.* **82** (1999) 4180 [hep-ph/9905212] [INSPIRE].

[172] C.-W. Chiang, Y.-T. Li and E. Senaha, *Revisiting electroweak phase transition in the standard model with a real singlet scalar*, *Phys. Lett. B* **789** (2019) 154 [arXiv:1808.01098] [INSPIRE].

[173] D. Croon, O. Gould, P. Schicho, T.V.I. Tenkanen and G. White, *Theoretical uncertainties for cosmological first-order phase transitions*, *JHEP* **04** (2021) 055 [arXiv:2009.10080] [INSPIRE].

[174] N.K. Nielsen, *On the Gauge Dependence of Spontaneous Symmetry Breaking in Gauge Theories*, *Nucl. Phys. B* **101** (1975) 173 [INSPIRE].

[175] R. Fukuda and T. Kugo, *Gauge Invariance in the Effective Action and Potential*, *Phys. Rev. D* **13** (1976) 3469 [INSPIRE].

[176] H.H. Patel and M.J. Ramsey-Musolf, *Baryon Washout, Electroweak Phase Transition, and Perturbation Theory*, *JHEP* **07** (2011) 029 [arXiv:1101.4665] [INSPIRE].

[177] C.-W. Chiang and E. Senaha, *On gauge dependence of gravitational waves from a first-order phase transition in classical scale-invariant* U(1)′ *models*, *Phys. Lett. B* **774** (2017) 489 [arXiv:1707.06765] [INSPIRE].

[178] P. Schicho, T.V.I. Tenkanen and G. White, *Combining thermal resummation and gauge invariance for electroweak phase transition*, *JHEP* **11** (2022) 047 [arXiv:2203.04284] [INSPIRE].

[179] L. Dolan and R. Jackiw, *Symmetry Behavior at Finite Temperature*, *Phys. Rev. D* **9** (1974) 3320 [INSPIRE].

[180] R.R. Parwani, *Resummation in a hot scalar field theory*, *Phys. Rev. D* **45** (1992) 4695 [hep-ph/9204216] [INSPIRE].

[181] M.E. Carrington, *The effective potential at finite temperature in the Standard Model*, *Phys. Rev. D* **45** (1992) 2933 [INSPIRE].

[182] W. Chao, *First order electroweak phase transition triggered by the Higgs portal vector dark matter*, *Phys. Rev. D* **92** (2015) 015025 [arXiv:1412.3823] [INSPIRE].

[183] M. Breitbach, J. Kopp, E. Madge, T. Opferkuch and P. Schwaller, *Dark, Cold, and Noisy: Constraining Secluded Hidden Sectors with Gravitational Waves*, *JCAP* **07** (2019) 007 [arXiv:1811.11175] [INSPIRE].

[184] D. Borah, A. Dasgupta and S.K. Kang, *Gravitational waves from a dark* U(1)D *phase transition in light of NANOGrav 12.5 yr data*, *Phys. Rev. D* **104** (2021) 063501 [arXiv:2105.01007] [INSPIRE].

[185] J.M. Cline and K. Kainulainen, *Electroweak baryogenesis and dark matter from a singlet Higgs*, *JCAP* **01** (2013) 012 [`arXiv:1210.4196`] [InSPIRE].

[186] V. Vaskonen, *Electroweak baryogenesis and gravitational waves from a real scalar singlet*, *Phys. Rev. D* **95** (2017) 123515 [`arXiv:1611.02073`] [InSPIRE].

[187] G. Kurup and M. Perelstein, *Dynamics of Electroweak Phase Transition In Singlet-Scalar Extension of the Standard Model*, *Phys. Rev. D* **96** (2017) 015036 [`arXiv:1704.03381`] [InSPIRE].

[188] J. Ellis, M. Lewicki and J.M. No, *On the Maximal Strength of a First-Order Electroweak Phase Transition and its Gravitational Wave Signal*, *JCAP* **04** (2019) 003 [`arXiv:1809.08242`] [InSPIRE].

[189] S. Biondini, P. Schicho and T.V.I. Tenkanen, *Strong electroweak phase transition in t-channel simplified dark matter models*, *JCAP* **10** (2022) 044 [`arXiv:2207.12207`] [InSPIRE].

[190] A.D. Sakharov, *Violation of CP Invariance, C asymmetry, and baryon asymmetry of the universe*, *Pisma Zh. Eksp. Teor. Fiz.* **5** (1967) 32 [InSPIRE].

[191] C.L. Wainwright, *CosmoTransitions: Computing Cosmological Phase Transition Temperatures and Bubble Profiles with Multiple Fields*, *Comput. Phys. Commun.* **183** (2012) 2006 [`arXiv:1109.4189`] [InSPIRE].

[192] J. Ellis, M. Lewicki, J.M. No and V. Vaskonen, *Gravitational wave energy budget in strongly supercooled phase transitions*, *JCAP* **06** (2019) 024 [`arXiv:1903.09642`] [InSPIRE].

[193] J. Ellis, M. Lewicki and J.M. No, *Gravitational waves from first-order cosmological phase transitions: lifetime of the sound wave source*, *JCAP* **07** (2020) 050 [`arXiv:2003.07360`] [InSPIRE].

[194] H.-K. Guo, K. Sinha, D. Vagie and G. White, *Phase Transitions in an Expanding Universe: Stochastic Gravitational Waves in Standard and Non-Standard Histories*, *JCAP* **01** (2021) 001 [`arXiv:2007.08537`] [InSPIRE].

[195] K. Schmitz, *New Sensitivity Curves for Gravitational-Wave Signals from Cosmological Phase Transitions*, *JHEP* **01** (2021) 097 [`arXiv:2002.04615`] [InSPIRE].

[196] A. Ringwald, K. Saikawa and C. Tamarit, *Primordial gravitational waves in a minimal model of particle physics and cosmology*, *JCAP* **02** (2021) 046 [`arXiv:2009.02050`] [InSPIRE].

[197] S. Banerjee, P.S.B. Dev, A. Ibarra, T. Mandal and M. Mitra, *Prospects of Heavy Neutrino Searches at Future Lepton Colliders*, *Phys. Rev. D* **92** (2015) 075002 [`arXiv:1503.05491`] [InSPIRE].

[198] P.J. Steinhardt, *Relativistic Detonation Waves and Bubble Growth in False Vacuum Decay*, *Phys. Rev. D* **25** (1982) 2074 [InSPIRE].